Modeling, System Identification, and Control for Dynamic Locomotion of the LittleDog Robot on Rough Terrain

by

Michael Yurievich Levashov

B.S. Aerospace Engineering,
B.S. Physics
University of Maryland (2008)

Submitted to the Department of Aeronautics and Astronautics
in partial fulfillment of the requirements for the degree of

Master of Science in Aeronautics and Astronautics

at the

MASSACHUSETTS INSTITUTE OF TECHNOLOGY

February 2012

Signature of Author .....
Department of Aeronautics and Astronautics
September 21, 2012

Certified by .....
Russ L. Tedrake
Associate Professor of Computer Science and Engineering
Thesis Supervisor

Accepted by .....
Eytan H. Modiano
Associate Professor of Aeronautics and Astronautics
Chair, Graduate Program Committee

Modeling, System Identification, and Control for Dynamic Locomotion of the LittleDog Robot on Rough Terrain

by

Michael Yurievich Levashov

Submitted to the Department of Aeronautics and Astronautics
on September 21, 2012, in partial fulfillment of the
requirements for the degree of
Master of Science in Aeronautics and Astronautics

Abstract

In this thesis, I present a framework for achieving a stable bounding gait on the LittleDog robot over rough terrain. The framework relies on an accurate planar model of the dynamics, which I assembled from a model of the motors, a rigid body model, and a novel physically-inspired ground interaction model, and then identified using a series of physical measurements and experiments. I then used the RG-RRT algorithm on the model to generate bounding trajectories of LittleDog over a number of sets of rough terrain in simulation. Despite significant research in the field, there has been little success in combining motion planning and feedback control for a problem that is as kinematically and dynamically challenging as LittleDog. I have constructed a controller based on transverse linearization and used it to stabilize the planned LittleDog trajectories in simulation. The resulting controller reliably stabilized the planned bounding motions and was relatively robust to significant amounts of time delays in estimation, process and estimation noise, as well as small model errors. In order to estimate the state of the system in real time, I modified the EKF algorithm to compensate for varying delays between the sensors. The EKF-based filter works reasonably well, but when combined with feedback control, simulated delays, and the model it produces unstable behavior, which I was not able to correct. However, the close loop simulation closely resembles the behavior of the control and estimation on the real robot, including the failure modes, which suggests that improving the feedback loop might result in bounding on the real LittleDog. The control framework and many of the methods developed in this thesis are applicable to other walking systems, particularly when operating in the underactuated regime.

Thesis Supervisor: Russ L. Tedrake
Title: Associate Professor of Computer Science and Engineering

Acknowledgments

I want to thank my adviser, Russ Tedrake, for having me as a student in his lab and providing me with the opportunity to do research in one of the best academic environments in the world. His teaching and guidance were invaluable during my time in the Robot Locomotion Group.

I want to also thank Alek Shkolnik, with whom I closely worked on LittleDog. He was extremely helpful in bringing me up to speed with the robot, we shared many ideas and lines of code for our research, and his ability to quickly hack together code worked well in combination with my thoroughness.

The Robot Locomotion Group has a great intellectual atmosphere, a can-do attitude, and is full of brilliant and always willing to help people. I want to thank all of the current and former members of RLG who helped me flesh out ideas, explained and discussed control algorithms, or even just temporarily took my mind off work with a random math problem.

Finally, I want to thank my family and friends for always supporting me in my pursuit of higher learning.

Contents

List of Figures

Chapter 1

Introduction

1.1 Motivation

Legged robots are capable of navigating over a much wider variety of terrains than wheeled robots, as illustrated in Figure 1-1 borrowed from [38]. The figure shows the legged robot navigating across gaps, up steps, and on steep slopes, which is not possible for a similar wheeled robot. In addition, the extra degrees of freedom available to a legged robot allow it to come back from otherwise unrecoverable states. These advantages are further amplified by the design of human environments, which are typically made accessible to bipedal humans, and might not always permit wheeled vehicles. A common, but not the only case, are stairs, which are ubiquitous in modern architecture.

Despite the advantages in their ability to navigate difficult terrain, legged robots have seen little practical use, mostly because of increased complexity that requires more careful design of the robot and the control method. Legged robots are faced with the challenges of dealing with changing configurations during walking or running motions, and of having to carry a large number of actuators that are typically used intermittently and have widely varying loads. Because of these constraints and limits on how much actuation can be reasonably carried, torque and velocity limits are usually important constraints for these robots, making the already non-linear dynamics even more complex to model and control. At every step, a legged robot has to deal

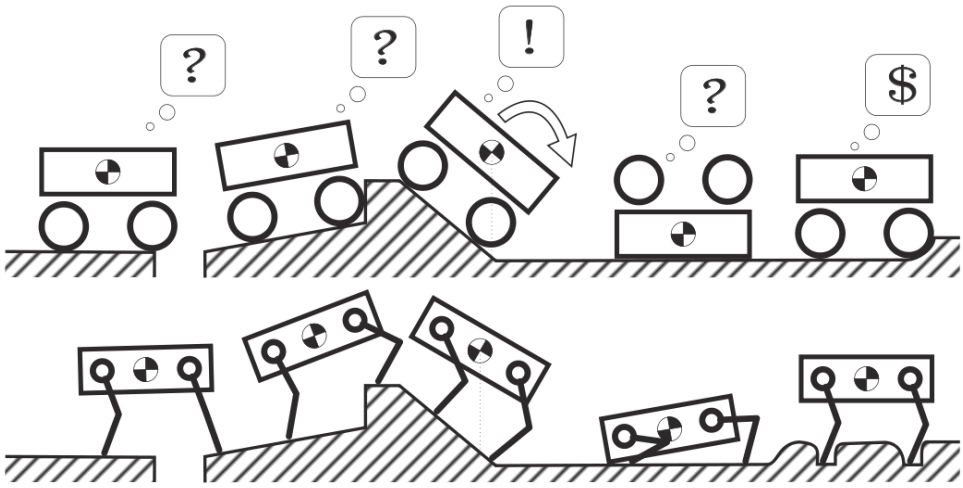

Figure 1-1: Advantages of legged over wheeled locomotion
Figure borrowed from [38]. Legged robot navigating over gaps, up steps, on steep inclines, and recovering from falls, which is not possible with a similar wheeled robot.

with ground impacts, which are difficult to model, because of their stochastic nature and dependence on the state of the robot, as well as on the properties of the foot and the ground it is stepping on. Finally, bipedal robots and quadruped robots using fast gaits both have to deal with underactuated dynamics, which can't be controlled directly and require more careful planning and execution of trajectories.

1.2 State of Legged Locomotion

There have been a number of impressive results in legged locomotion, particularly on the hardware side, and arguably the most success has been seen in robots that were carefully designed to generate walking or running motions with simplistic and intuitive control.

A good example of this are the robots developed in the MIT Leg Lab and later at Boston Dynamics ([37],[36],[35]). These robots rely on using large amount of actuation to make them behave like a one-legged hopping robot, which is well understood and can be effectively controlled with simple techniques. However, these simplifications rely on a particular design of the robot, are quite power intensive, and typically can't use information about external terrain, significantly limiting their robustness and

undermining one of the main motivations for legged locomotion.

On the opposite side of the spectrum, a number of researchers have been studying robots whose natural dynamics permit them to walk passively downhill [29]. These robots inspired a lot of research into the dynamics of simple walking models to understand what enables stable passive walking, stabilize it for flat terrains by adding small amounts of actuation, and imitate these gaits ([10],[11],[12],[41],[51],[1],[47],[8]). Although this approach typically results in highly energy-efficient locomotion as well as "natural-looking" gaits, it was found to be difficult to generalize to other robots, to make it work for terrains with significant roughness, or be robust to uncertainties in system dynamics or the terrain.

The control of some robots have relied on high-gain actuation at the joints and carefully planned trajectories that keep the robot within its region of static stability or within its dynamic generalization with the Zero Moment Point (ZMP) concept [50]. This is the preferred method of controlling most humanoid robots ([19],[21]), including Honda's Asimo ([39],[14]), as well as many other ones, such as the quadruped LittleDog developed by Boston Dynamics. These robots, unlike the ones mentioned above, are capable of taking advantage of terrain knowledge to leverage the power of legged locomotion, but typically suffer from having energetically inefficient gaits and are highly constrained in their selection of possible motions.

To allow for more dynamically rich motions to enhance mobility, while requiring less actuation effort, some approaches rely on controlling intuitive quantities, such as the angular momentum [18], or on using hand-tuned or carefully optimized periodic gaits ([17],[38]).

When accurate models are available, direct design of trajectories in the state space of a robot is very promising for legged locomotion, as it is widely applicable across many walking platforms, has the potential to fully exploit the potential dynamic motions of the robot, while allowing the designer to put a weight on power efficiency, and makes it possible to incorporate knowledge of the terrain into the trajectories. To keep the robot from deviating from these trajectories usually requires good feedback, and a number of such feedback controllers have been developed and successfully tested

on real robots ([2],[42],[6],[52],[48]). One of these controllers, transverse linearization, has been recently successfully used to stabilize trajectories for a number of simple walking models and real robots ([43],[24]). In this work, we apply the idea of trajectory optimization with transverse linearization to the significantly more challenging task of generating stable bounding of Boston Dynamic's LittleDog over rough terrain.

1.3 LittleDog

The "Learning Locomotion" program [33] was a DARPA project that provided a number of university research teams with a set of rough terrains and the LittleDog robot [30], designed for this purpose by Boston Dynamics. The goal of the project was to plan and navigate over these terrains as quickly as possible with LittleDog in the environment of good off-board position estimation and perfect terrain knowledge.

The LittleDog robot, shown in Figure 1-2, is a stiff quadruped with servo motors at every joint. This gives the robot the capability of accurate foot placement, but restricts the possible dynamically interesting motions, because of lack of ways to store significant potentially energy, such as in springs, or kinetic energy aside from in the main body of the robot. Because of these hardware constraints, the teams mostly focused on careful planning or learning and execution of trajectories with ZMP or similar approaches and high-gain feedback ([22],[53],[31],[20],[44],[34]).

Midway through and towards the end of the project, some teams started to successfully incorporate more dynamically rich motion segments into their planned trajectories, allowing them to travel faster and traverse more difficult terrain ([4],[22],[53]). These segments, being dynamically unstable, had to be kept short and end with statically stable states that would funnel possible deviations from the nominal to a known state, so that the planned trajectory could be continued.

In this work we present how, inspired by these approaches, we developed a dynamical model of LittleDog and used trajectory optimization and stabilization to eliminate the statically stable parts from LittleDog motion plans to achieve continuous bounding in simulation. Bounding motions on LittleDog are subject to motor

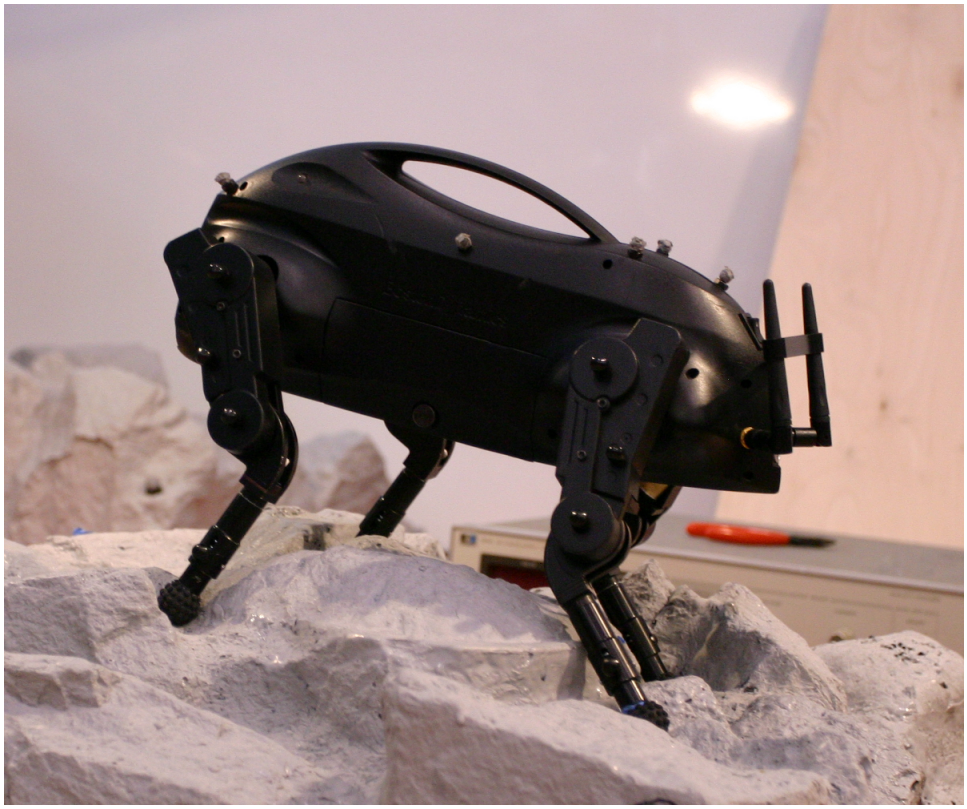

Figure 1-2: The LittleDog robot on a rock terrain
LittleDog is a stiff quadruped robot developed by Boston Dynamics.

saturations, impacts, and underactuated dynamics, capturing many of the difficulties of legged locomotion, making these methods applicable across many walking robots.

1.4 Contributions

In this work, we develop and identify an accurate dynamical model of the LittleDog robot that combines simple models of the robot's motors and links, as well as a novel ground interaction model. Using the model, we construct an estimator for LittleDog, based on the Extended Kalman Filter, but modified to carefully correct for delays in the sensing. We discuss the effects of having large control time steps on transverse linearization and then construct an algorithm for applying LQR with transverse linearization in this context. We then demonstrate successful robust bounding of the LittleDog robot across a wide variety of terrains in simulation.

The work is organized as follows. In Chapter 2 we provide a more detailed overview of our approach for stabilizing LittleDog bounding. Chapter 3 presents the planar dynamic model of the robot and its identification procedure. Chapter 4 goes into detail about the state estimator, while Chapter 5 goes into detail about the feedback controller. Chapter 6 presents our result of stable bounding in simulation, the issues arising from feedback between the control and estimation algorithms and discusses our attempts to make the approach work on the real robot. Finally, Chapter 7 provides a summary of this work and discusses potential future improvements.

Chapter 2

Framework

Figure 2-1 shows the approach taken in this work to achieve bounding locomotion of LittleDog over rough terrain.

In general, the task of a locomotion algorithm is to move the robot from a start position to the desired goal position by computing an appropriate set of motor commands based on the sensor readings. To keep the dimensionality of the state space as low as possible, making the task more tractable, while still allowing some capability for interesting dynamical motions, we chose to restrict the LittleDog dynamics to the sagittal plane. This was accomplished by constraining the front pair as well as the back pair of legs to move in unison and making the height of the terrain invariant with respect to the direction orthogonal to LittleDog's plane of motion. The constraint makes a bounding gait the only practical method of navigating for the robot, since, unless it drags its feet for the whole distance, it is forced to alternate between lifting the front and back legs.

The number of possible dynamical states of the robot is large, its motions are sensitive to deviations in the states and inputs as well as to external disturbances, the sensor readings are subject to noise, and it is not in general possible to bring the robot into a desired dynamical state directly. For that reason, directly learning the motor commands that will robustly take the robot from the start to the goal is computationally prohibitive. Even if it was accomplished, a small change to the robot's dynamics or the terrain would, in general, require the commands to be relearned from

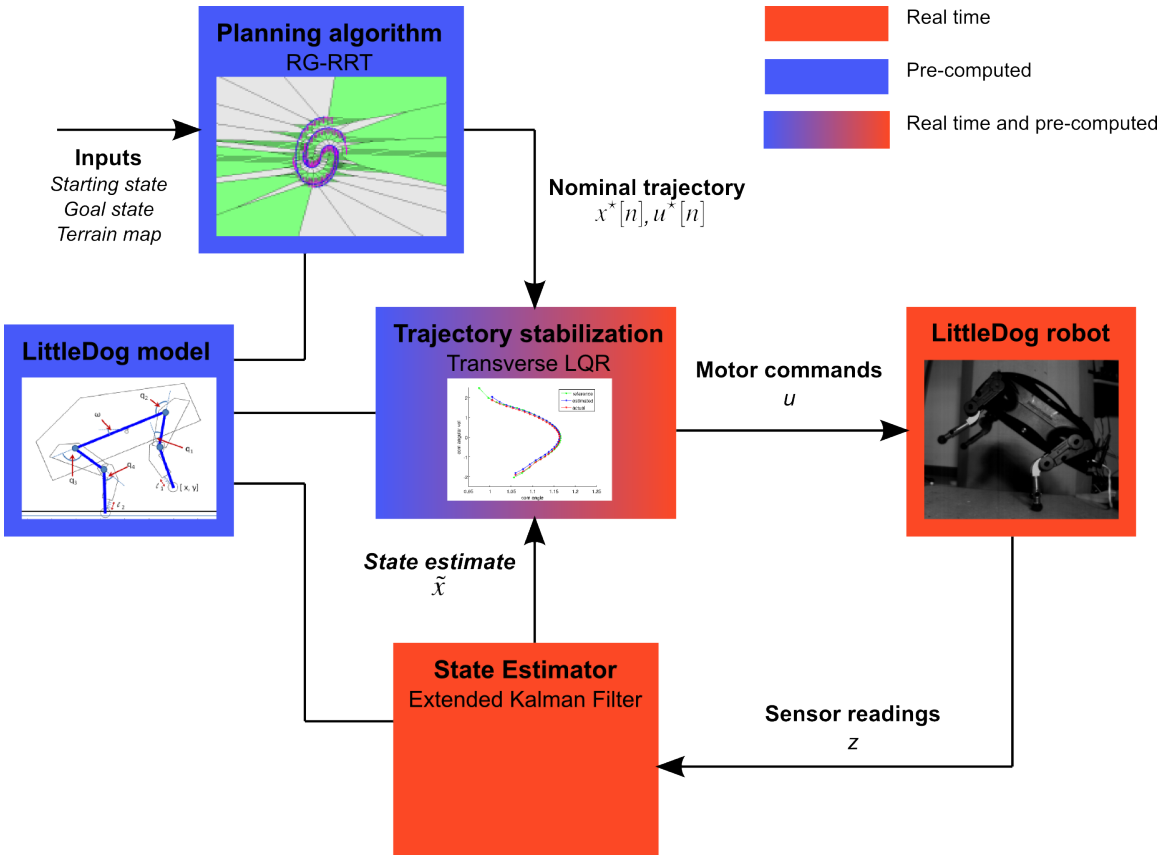

Figure 2-1: LittleDog bounding control framework

The planning algorithm creates a feasible trajectory from the start to the goal states for a given terrain. A set of gains is computed for the trajectory and used in a real-time control and estimation feedback loop to stabilize the robot. The planning, estimation, and control portions rely on an accurate dynamical model of LittleDog.

scratch. The alternative to directly learning the commands is model-based control. We have developed a physics-based model that allows us to predict the response of LittleDog to a given set of commands, making it possible to develop a control policy without directly exploring all possible configurations on the physical robot. As seen in Figure 2-1, most parts of the bounding algorithm rely on the model's predictions. We use a model based on multiple rigid-body links, with motor dynamics at the joints and a novel ground contact model. Chapter 3 goes into detail about the structure of the model and the methods used to identify its parameters.

To further simplify the bounding task, we employ a standard control systems approach of separating the feedback control and estimation problems. The estimation algorithm computes a state estimate based on the previous estimate, sensor readings, and a model of the robot's sensors and passes it to the feedback control algorithm, so the latter can be designed in the state space of the model instead of the space of all possible stochastic sensor histories. This simplification tends to work well as long as errors in the state estimate are sufficiently small to not destabilize the overall system. For state estimation we use an Extended Kalman Filter with a few alterations to accommodate for time delays. A detailed description of LittleDog sensors and the relevant time delays, the EKF implementation, and an evaluation of its performance are given in Chapter 4.

Even with the simplifications listed above, for a complex dynamical system such as LittleDog it is not practical (or even feasible, since it is impossible to recover from certain states) to produce a valid control policy for every possible state. Luckily, this is not necessary when only a small fraction of the state space is expected to be visited. In this work, we use a common approach of computing a feasible trajectory of states from the starting state to an end state inside the goal region and a set of motor commands that generate the trajectory. This is accomplished by the RG-RRT algorithm ([46], [45]), which was able to plan trajectories over a wide variety of terrains. The RG-RRT algorithm starts from the initial state and constructs a tree that sparsely explores the reachable states, while pruning out states that result in collisions or don't meet certain heuristics. The tree is constructed by randomly sampling motion primitives for motor

commands and using the LittleDog model presented in Chapter 3 to compute the state transitions for these primitives. The output of the planning algorithm is a trajectory of states and a set of motor commands that, when executed on the robot starting from the initial state, will cause it to go through the states of the trajectory and end up at the goal state.

However, when executed on a real physical system, because of stochastic disturbances and imperfections in the modeling, the actual trajectory might diverge arbitrarily far from the theoretical one. Model Predictive Control [28] solves this by computing a new trajectory at every timestep, but this is, in general, computationally expensive and might not be possible to do in real time. For example, for LittleDog, computing a feasible trajectory to the goal with RG-RRT takes on the order of 10 minutes. A more efficient approach is to compute, for states close to the original trajectory, an adjustment to the motor commands to keep the system near the original path. If the controller can effectively deal with the perturbations, the system will remain near the trajectory and will eventually reach a region close to the goal, as desired. We accomplish this by applying transverse linearization techniques to the trajectories, as explained in Chapter 5. This is done by re-parametrizing the trajectories, constructing a new coordinate system that is transverse to the dynamics, and controlling the transverse dynamics using a gain-scheduling controller based on the LQR cost function.

Chapter 3

Model

An essential component of any model-based planning approach is a sufficiently accurate identification of the system dynamics. Obtaining an accurate dynamic model for LittleDog is challenging due to subtleties in the ground interactions and the dominant effects of motor saturations and transmission dynamics. These effects are more pronounced in bounding gaits than in walking gaits, due to the increased magnitude of ground reaction forces at impact and the perpetual saturations of the motor; as a result, we required a more detailed model. In this section, we describe our system identification procedure and results.

The LittleDog robot has 12 actuators (two in each hip, one in each knee) and a total of 22 essential degrees of freedom (six for the body, three rotational joints in each leg, and one prismatic spring in each leg). By assuming that the leg springs are over-damped, yielding first-order dynamics, we arrive at a 40 dimensional state space $(18 \times 2 + 4)$. However, to keep the model as simple (low-dimensional) as possible, we approximate the dynamics of the robot using a planar 5-link serial rigid-body chain model, with revolute joints connecting the links, and a free base joint, as shown in Figure 3-1. The planar model assumes that the back legs move together as one and the front legs move together as one. Each leg has a single hip joint, connecting the leg to the main body, and a knee joint. The foot of the real robot is a rubber-coated ball that connects to the shin through a small spring (force sensor), which is constrained to move along the axis of the shin. The spring is stiff, heavily damped, and has a

limited travel range, so it is not considered when computing the kinematics of the robot, but is important for computing the ground forces. In addition, to reduce the state space, only the length of the shin spring is considered. This topic is discussed in detail as part of the ground contact model.

The model's 7-dimensional configuration space, $\mathcal{C} = \mathbb{R}^2 \times \mathbb{T}^5$, consists of the planar position of the back foot (x, y), the pitch angle ω, and the 4 actuated joint angles $q_1, ..., q_4$. The full state of the robot, $x = [\mathbf{q}, \dot{\mathbf{q}}, \mathbf{l}] \in \mathcal{X}$, has 16 dimensions and consists of the robot configuration, the corresponding velocities, and the two prismatic shin-spring lengths, $\mathbf{l} = [l_1, l_2]$, one for each foot. The control command, $\mathbf{u}$, specifies reference angles for the 4 actuated joints. The robot receives joint commands at 100 Hz and then applies an internal PD controller at 500 Hz. For simulation, planning

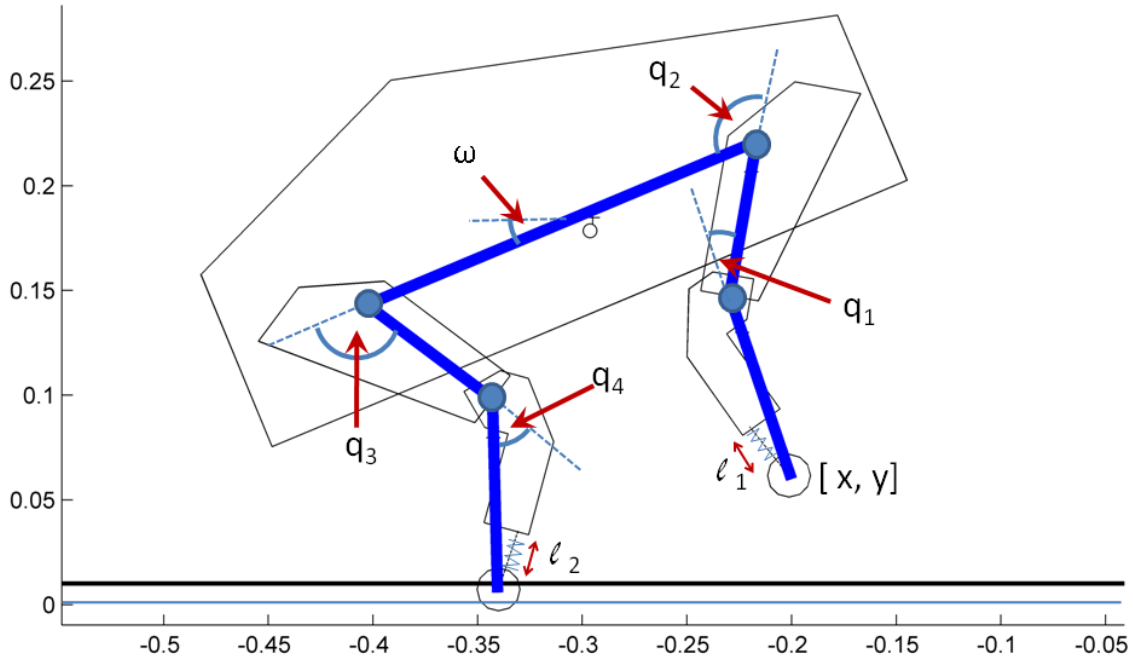

Figure 3-1: LittleDog model
The state space is $\mathcal{X} = [\mathbf{q}, \dot{\mathbf{q}}, \mathbf{l}]$, where $q = [x, y, \omega, q_1, q_2, q_3, q_4]$, and $\mathbf{l} = [l_1, l_2]$ are feet spring lengths used in the ground contact model. The diagram also illustrates the geometric shape of the limbs and body, information used for collision detection during planning.

and control purposes, the dynamics are defined as

$$\mathbf{x}[n+1] = f(\mathbf{x}[n], \mathbf{u}[n]), \tag{3.0}$$

where $\mathbf{x}[n+1]$ is the state at $t[n+1]$, $\mathbf{x}[n]$ is the state at $t[n]$, and $\mathbf{u}[n]$ is the actuated joint position command applied during the time interval between $t[n]$ and $t[n+1]$. We will sometimes refer to the control time step, $\Delta T = t[n+1] - t[n] = 0.01$ seconds. A fixed-step 4th order Runge-Kutta integration of the continuous Euler-Lagrange dynamics model is used to compute the state update.

A self-contained motor model is used to describe the movement of the actuated joints. Motions of these joints are prescribed in the 5-link system, so that as the dynamics are integrated forward, joint torques are back-computed, and the joint trajectory specified by the model is exactly followed. This model is also constrained so that actuated joints respect bounds placed on angle limits, actuator velocity limits, and actuator torque limits. In addition, forces computed from a ground contact model are applied to the 5-link chain when the feet are in contact with the ground. The motor model and ground contact forces are described in more detail below. The actuated joints are relatively stiff, so the model is most important for predicting the motion of the unactuated degrees of freedom of the system, in particular the pitch angle, as well as the horizontal position of the robot.

3.1 Motor Model

The motors on LittleDog have gear ratios of approximately 70 : 1. Because of the high gear ratio, the internal second-order dynamics of the individual motors dominate in most cases, and the rigid-body dynamics of a given joint, as well as effects of inertial coupling and external forces on the robot can be neglected. The combination of the motor internal dynamics with the PD controller with fixed PD gains can be accurately modeled as a linear second-order system:

$$\ddot{q}_i = -b\dot{q}_i + k(u_i - q_i), \tag{3.0}$$

where $\ddot{q}_i$ is the acceleration applied to the i^{th} joint, given the state variables $[q_i, \dot{q}_i]$ and the desired position u_i. To account for the physical limitations of actual motors, the model includes hard saturations on the velocity and acceleration of the joints. The velocity limits, in particular, have a large effect on the joint dynamics in practice.

Each of the 4 actuated joints is assumed to be controlled by a single motor, with both of the knee joints having one pair of identical motors, and the hip joints having a different pair of identical motors (the real robot has a differential in the hip, but not the knee). Because of this, two separate motor parameter sets: $\{b, k, v_{lim}, a_{lim}\}$ are used, one for the knees, and one for the hips. The velocity limits of the joints, v_{lim}, are the result of counter EMF in the DC motors. When the acceleration limits, a_{lim} are reached, the response is non-smooth and results in the motors stuttering, which is not practical to model. This suggests that a_{lim} are a result of current failsafes in LittleDog's electronics, but it is not possible to confirm that because of lack of access to the robot's internals. In agreement with the guess, a_{lim} depends on the amount of load on the joints of the robot, but is modeled to be constant for simplicty. Increasing the external power supply voltage increases a_{lim} and reduces the stuttering, so for all experiments the voltage was set to $20V$, which is the maximum allowed value according to LittleDog specifications.

Figure 3-2 shows a typical fit of the motor model to motor encoder readings, collected from a number of bounding gaits. The fits are consistent across the different joints of the robot and across different LittleDog robots, but depend on the gains of the PD controller at each of the joints. As seen from the figure, the motor model does well in tracking the actual joint position and velocity. Under large dynamic loads, such as when the hip is lifting and accelerating the whole robot body at the beginning of a bound, the model might slightly lead the actual joint readings. This can be seen in Figure 3-2 (top) at 5.4 s. For the knee joint and for less aggressive trajectories with the hip, the separation is not significant. Additionally, note that backlash in the joints is not modeled. The joint encoders are located on the motors rather than the joint axes, which makes it very difficult to measure and model backlash.

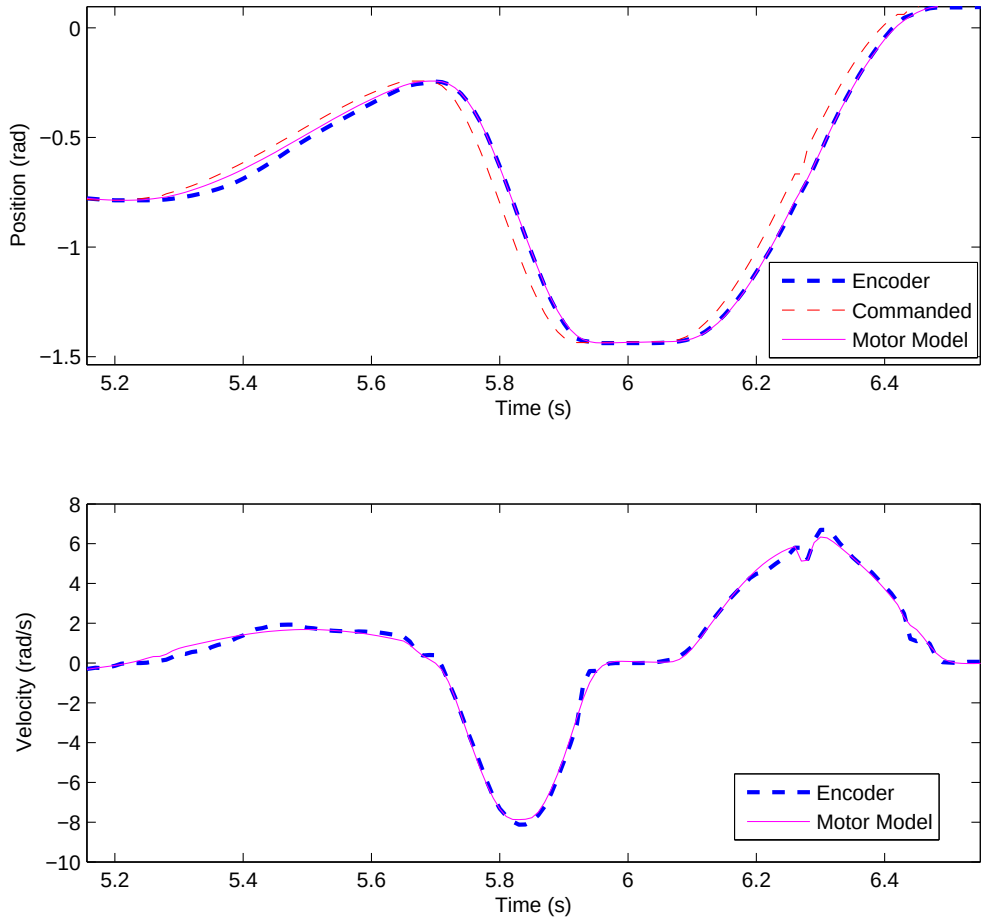

Figure 3-2: Example of a hip joint trajectory
The position command is shown in thin dashed red, the motor model prediction is shown in solid magenta, and actual encoder reading is in thick dashed blue.

3.2 Ground Interaction Model

LittleDog is mostly incapable of an aerial phase due to the velocity limits in the joints, so at least one foot is usually in contact with the ground at any time. The ground interaction is complicated, because the robot's foot may roll, slide, stick, bounce, or do some combination of these.

Ground contact models can be discrete or continuous (see [9] for an overview.) Discrete collision modeling can range from using a constant coefficient of elasticity to more advanced approaches that can predict slipping behavior and the presence or

absence of bounce [3]. Discrete modeling is advantageous because of its simplicity, but is not well suited for LittleDog, because it assumes an instantaneous change in momentum, whereas on the robot compression of shin springs extends the collision duration to a time-scale comparable with the rest of LittleDog dynamics. Continuous impact modeling is more suited for LittleDog and can be subdivided into modeling the forces normal and tangential to the surface. The ground contact model presented here carefully computes the interaction of LittleDog feet with rough terrain, allowing it to predict shin-spring displacement, foot roll, foot slip, compliance and energy dissipation during ground collision, and bounce when too little energy is dissipated.

A continuous, elastic ground interaction model is used, where the foot of the robot is considered as a ball, and at each point in time the forces acting on the foot are computed. The ground plane is assumed to be compressible, with a stiff nonlinear spring damper normal to the ground that pushes the foot out of the terrain. A tangential friction force, based on a nonlinear model of Coulomb friction is also assumed. The normal and friction forces are balanced with the force of the shin spring at the bottom of the robot's leg. The rate of change of the shin spring, $\dot{\mathbf{l}}$, is computed by the force balancing and used to update the shin-spring length, $\mathbf{l}$, which is a part of the state space. The resulting normal and friction forces are applied to the 5-link model.

3.2.1 Terrain Model and Foot Roll

The feet on LittleDog are small rubber balls about 2 cm in diameter. When the angle of the leg to the terrain changes, the ball rolls, producing a noticeable displacement. This is equivalent to a movement of the ball's center along a different terrain, which is offset from the original by the foot radius. To account for this effect, given a terrain height map, $\gamma(x)$, a new terrain height map, $\gamma^*(x)$, is computed such that every point on it is exactly one ball radius, r_b, away from the original terrain:

$$\begin{aligned} &r_b = \min_z \left\{(\gamma^*(x) - \gamma(z))^2 + (x - z)^2\right\}, \forall x \\ &\gamma^*(x) > \gamma(x), \forall x \end{aligned} \tag{3.0}$$

Both height maps can be seen in Figure 3-1, where the bottom light blue horizontal line is $\gamma(x)$, the original terrain, and the black line above it is $\gamma^*(x)$, the terrain computed by Equation (3.2.1). In this case, $\gamma^*(x) = \gamma(x) + r_b$, but this is not generally true for non-flat terrain.

When a LittleDog foot rolls, the velocity of the foot center is different from the velocity at the ground contact by $r_b\dot{\theta}$, where $\dot{\theta}$ is the absolute angular velocity of the foot. The new height map and the adjustment to ground contact velocity completely capture the foot roll behavior.

All ground contact computations use the new height map, $\gamma^*(x)$, referred to as 'the terrain' below. A function for the slope of the terrain, $\alpha(x)$, is computed from $\gamma^*(x)$.

3.2.2 Ground Friction Model

The friction force between the ground and the feet is assumed to be a smooth function of velocity and to be tangent to the ground surface:

$$\frac{F_f}{N} = K_f \arctan\left(K_d \dot{s}\right). \tag{3.0}$$

Here, F_f is the friction force, N is the surface normal force, $\dot{s}$ is the ground contact velocity, K_f and K_d are model parameters.

To fit the data, the robot was commanded to hold its legs straight and placed on an inclined surface. The steady-state velocity (from Motion Capture) as well as the normal and tangential forces (computed from a steady sliding assumption) were measured for a variety of slopes and are shown in Figure 3-3, along with a fit of the friction model.

For high magnitudes of velocity, the friction force equation resembles that of Coulomb friction. As the magnitude decreases, the force drops off to smoothly change direction at 0 velocity. The smoothness of the function is important for integration purposes and seems to be a good approximation except for extremely small velocities. At small velocities, the friction coefficient is small and might produce drift, but it is

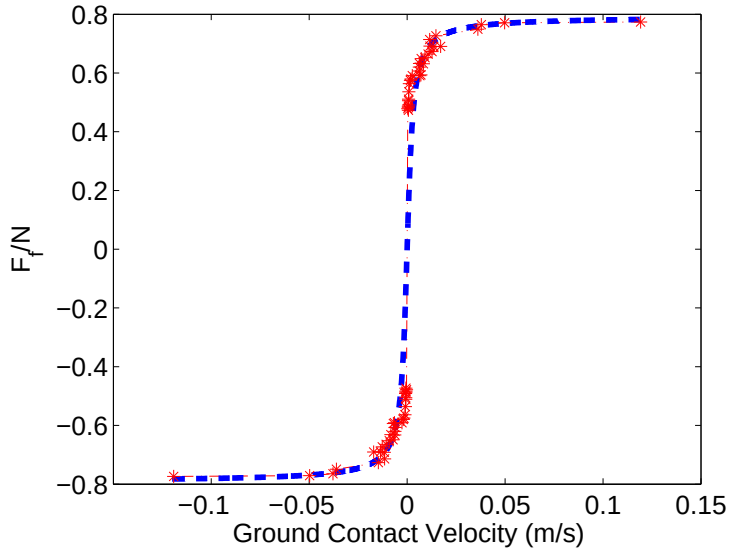

Figure 3-3: Friction coefficient fit
Friction coefficient versus steady state velocity on an inclined plane.

negligible in typical timescales of a simulation run (less than 1 minute). An arctangent was selected for the functional form because it fits the available data well, but other sigmoids could be used.

3.2.3 Ground Forces Computation

A diagram of a foot in collision with flat terrain is shown in Figure 3-4. The figure shows a portion of the robot shin in top right, connected to the shin spring of length l, which is modeled as a non-linear spring-damper. Connected to the shin spring is the foot, the center of which is shown below the ground in the figure at position $[p_x, p_y]$. The center of each foot is computed from the current state of the robot. Whenever a foot center $[p_x, p_y]$ is below the terrain, $p_y < \gamma^*(p_x)$, the foot is considered to be in collision.

The foot below the shin spring is assumed to be massless. Therefore, the sum of forces acting on it is zero and is given by

$$\vec{F}_f + \vec{N} + \vec{M} + \vec{P} = 0, \tag{3.0}$$

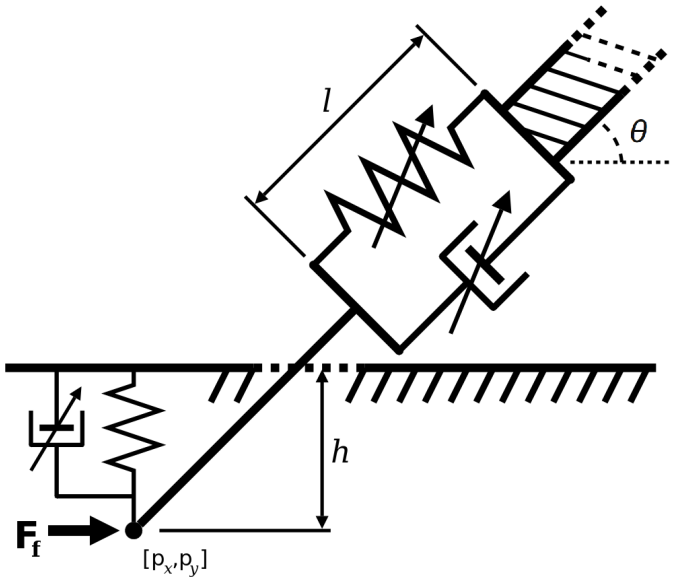

Figure 3-4: Ground Contact Model
A foot with a center at $[p_x, p_y]$ is attached to a shin spring of length l at an angle of θ to the terrain. The foot penetrates a distance h into the ground, which is modeled as a compressible plane. A velocity-dependent friction force is applied at the point of ground contact. The terrain angle at the ground contact point is equal to α, and is not shown in the figure.

where F_f is the friction force, N is the normal force, M is the shin-spring force, and P is the perpendicular force applied on the foot by the spring housing.

The normal force model uses a non-linear spring-damper of the form introduced by [16]:

$$N = K_h h(1 - \zeta_h \dot{h}), \tag{3.0}$$

where h is the penetration depth, $\dot{h}$ is the rate of change of the penetration, and K_h and ζ_h are constants. Compared to linear damping, it has the advantage of being continuous across the ground contact and avoiding sticking forces between surfaces for almost all cases [26]. The penetration depth, h is computed as the shortest distance between the foot center and the height map, $\gamma^*(x)$, and is perpendicular to the height map. Since on the actual robot the foot can't overlap the terrain, it is assumed that any overlap is due to compliance in the leg, the rubber foot or the ground.

Note that $\dot{h}$ is an algebraic function of $[\dot{p_x}, \dot{p_y}]$, the foot center velocity, which in turn is an algebraic function of the known robot state and $\dot{l}$. Unlike l, $\dot{l}$ is not a part

of the state, so $\dot{h}$ can't be computed directly. The normal force is affine in $\dot{l}$, so, for a robot in state x, Equation (3.2.3) can be rewritten as

$$N = N_x(x) + N_l(x)\dot{l}, \tag{3.0}$$

where $N_x(x)$ an $N_l(x)$ are non-linear functions of the state.

The actual shin spring on the robot is limited in its range of travel. During a bounding motion, it is typical for the spring to reach the limits of motion, where it hits a hard stop. The spring is modeled as linear in its normal range and to have a hard collision at the travel limits of the same functional form as the normal force. Assuming a rest length of l_0, the displacement from rest is $\delta l = l - l_0$, and the range of travel for δl is between 0 and l_{max}, the force is given by

$$M = \begin{cases} K_s\delta l + b_s\dot{l} + K_c\delta l(1 + \zeta_l\dot{l}), & \delta l < 0 \\ K_s\delta l + b_s\dot{l}, & 0 \leq \delta l < l_{max} \\ K_s\delta l + b_s\dot{l} + K_c(\delta l - l_{max})(1 - \zeta_l\dot{l}), & l_{max} \leq \delta l \end{cases} \tag{3.0}$$

where K_s and $K_c \gg K_s$ are stiffness parameters, b_s and ζ_l are damping parameters. Similarly to the normal force, the spring force is affine in $\dot{l}$ and can be written as

$$M = M_x(x) + M_l(x)\dot{l} \tag{3.0}$$

for some nonlinear functions of the state $M_x(x)$ and $M_l(x)$.

The friction force is given by Equation (3.2.2), where $\dot{s}$ is the velocity of the foot center along the height map $\gamma^*(x)$ and can be computed from the state of the robot x, the slope of the terrain at the ground contact α, and $\dot{l}$.

The force applied to the foot by the spring housing, P, is unknown, but can be eliminated from the force balance by only considering the component of Equation (3.2.3) that is orthogonal to P. Noting that $M \perp P$, $F_f \perp N$, the angle between the

spring and the ground is $\theta - \alpha$, and substituting (3.2.2) into (3.2.3) gives

$$\begin{aligned} 0 &= F_f \cos(\theta - \alpha) + N(x, \dot{l}) \sin(\theta - \alpha) - M(x, \dot{l}) \\ &= [K_f \arctan\left(K_d \dot{s}(x, \dot{l}) \cos(\theta - \alpha)\right) + \sin(\theta - \alpha)] N(x, \dot{l}) - M(x, \dot{l}) \end{aligned} \tag{3.0}$$

which is just a function of the robot state and $\dot{l}$, and where $N(x, \dot{l})$and $M(x, \dot{l})$ are given by Equations (3.2.3) and (3.2.3), respectively.

By approximating the arc-tangent function, Equation (3.2.3) is used to find $\dot{l}$, which is then used to find the normal and friction forces using Equations (3.2.3) and (3.2.2). The forces are then applied to the appropriate point of the rigid 5-link model and $\dot{l}$ is used to update the shin-spring length. Although for some parameters and system states, Equation (3.2.3) might have multiple solutions for $\dot{l}$, in practice, the $\dot{l}$ with the lower magnitude can be chosen as the physically plausible solution. All of the ground interaction forces are dissipative, so the dynamics are guaranteed to remain stable.

For a foot not in collision, no forces are applied on the foot, so $F_f = N = 0 \rightarrow M = 0$. The rate of change of the shin length is then, from Equation (3.2.3),

$$\dot{l} = -\frac{M_l(x)}{M_x(x)}, \tag{3.0}$$

which is a fast, stable non-linear system that drives l to l_0 quickly after the foot leaves the ground.

3.3 Parameter Estimation

There are many coupled parameters that determine the behavior of the model. In theory, they could all be fit to a large enough number of robot trajectories, but it would require thoroughly exploring relevant regions of the robot's {STATE-SPACE × ACTION-SPACE}. This is difficult, because LittleDog can't easily be set to an arbitrary point in state space, and the data we collect only covers a tiny fraction of it. An easier and more robust approach relies on the model structure to separate the fitting into sub-problems

and to identify each piece separately. The full dynamical model of the robot consists of the 5-link rigid body, the motor model, and the ground force model. A series of experiments, described below, and a variety of short bounding trajectories were used to fit the model parameters to actual robot dynamics by minimizing quadratic cost functions over simulation error. All of the fits were computed with nonlinear function optimization (using MATLAB's fminsearch).

In total, 34 parameters were measured or fit for the model. Table 3.1 lists the parameters and their values. In the table, the length of the shin is given from the knee joint to the foot center, assuming full extension of the shin spring. Centers of masses are given in the reference frames of their links, with x pointing along its link and y perpendicular to it in a right-handed convention. The origin of the back shin is at the back foot and $\hat{x}$ points toward the knee joint, the origin of the back upper leg is at the knee joint and its $\hat{x}$ points toward the hip joint, and the origin of the body is at the back hip joint, with its $\hat{x}$ pointing toward the front hip joint. The front links have mirror symmetry with the back legs.

The motor model was assumed to be independent of the other parameters and fit to real joint trajectory data. The fit accurately predicts the behavior of the joints, as seen in Figure 3-2, which shows the model performance on a different trajectory. The friction coefficients in the ground force model were fit to steady-state sliding as described in section 3.2.2. The rest of the ground contact model was identified by commanding the robot to hold its legs straight down, parallel to each other, dropping it vertically onto flat terrain, and fitting the parameters to the resulting body trajectory, measured with Motion Capture. The total mass of the robot, the lengths of each link, and the maximum shin spring travel were measured directly.

The remaining parameters, including inertias of the links, the mass distribution between the links, and center of mass locations, were fit to a large number of short bounding trajectories. The cost function for the fit was a quadratic form on the distance between actual and simulated feet positions, which captures the effect of the 3 unactuated variables (x, y, and body pitch), neglecting the unactuated shin springs that are not considered to be a part of the configuration.

For the rigid body model, the parameters are heavily coupled and some of the individual values might not be accurate. This is true of the inertias and to some degree of the centers of masses. Because the planar model lumps two LittleDog legs into a single leg, the leg masses and inertias, as well as some of the stiffnesses and damping values, are twice as large as their physical counterparts for a single leg.

3.3.1 Model Performance

Figure 3-5 shows a comparison of a bounding trajectory in simulation versus 10 runs of the same command executed on the real robot. The simulated trajectory was generated using the RG-RRT planning algorithm, which used the developed model. The control input and the starting conditions for all open-loop trajectories in the figure were identical, and these trajectories were not used for fitting the model parameters.

Three of the four plots are of an unactuated coordinate (x, y, and body pitch), the fourth one is of the back hip, an actuated joint. The figure emphasizes the difference between directly actuated, position controlled joints compared to unstable and unactuated degrees of freedom. While the motor model tracks the joint positions almost perfectly, even through collisions with the ground, the unactuated coordinates of the open-loop trajectories diverge from each other in less than 2 seconds. Right after completing the first bounding motion, at about 1.5 s, the trajectories separate as LittleDog is lifting its body on the back feet. At about 1.9 s, in half of the cases the robot falls forward and goes through a second bounding motion, while in the rest of the cases it falls backward and can't continue to bound. The horizontal position and body pitch coordinates are both highly unstable and unactuated, making it difficult to stabilize them. The control problem is examined in more detail later in this paper.

The most significant unmodeled dynamics in LittleDog include backlash, stiction in the shin spring, and more complex friction dynamics. For example, even though the friction model fits well to steady-state sliding of LittleDog, experiments on the robot show that during a bounding motion there are high-frequency dynamics induced in the legs that reduce the effective ground friction coefficient. Also, the assumption of

linearity in the normal force in Coulomb friction does not always hold for LittleDog feet. Modeling these effects is possible, but would involve adding a large number of additional states with nonlinear high-frequency dynamics to the model, making it much harder to implement and less practical overall. In addition, the new states would not be directly observable using currently available sensors, so identifying the related parameters and initializing the states for simulation would be difficult.

In general, for a complex unstable dynamical system such as LittleDog, some unmodeled effects will always remain no matter how detailed the model gets. Instead of capturing all of the effects, the model approximates the overall behavior of the system, as seen from Figure 3-5. We believe that this model is sufficiently accurate to generate relevant motion plans in simulation which can be stabilized using feedback on the real robot.

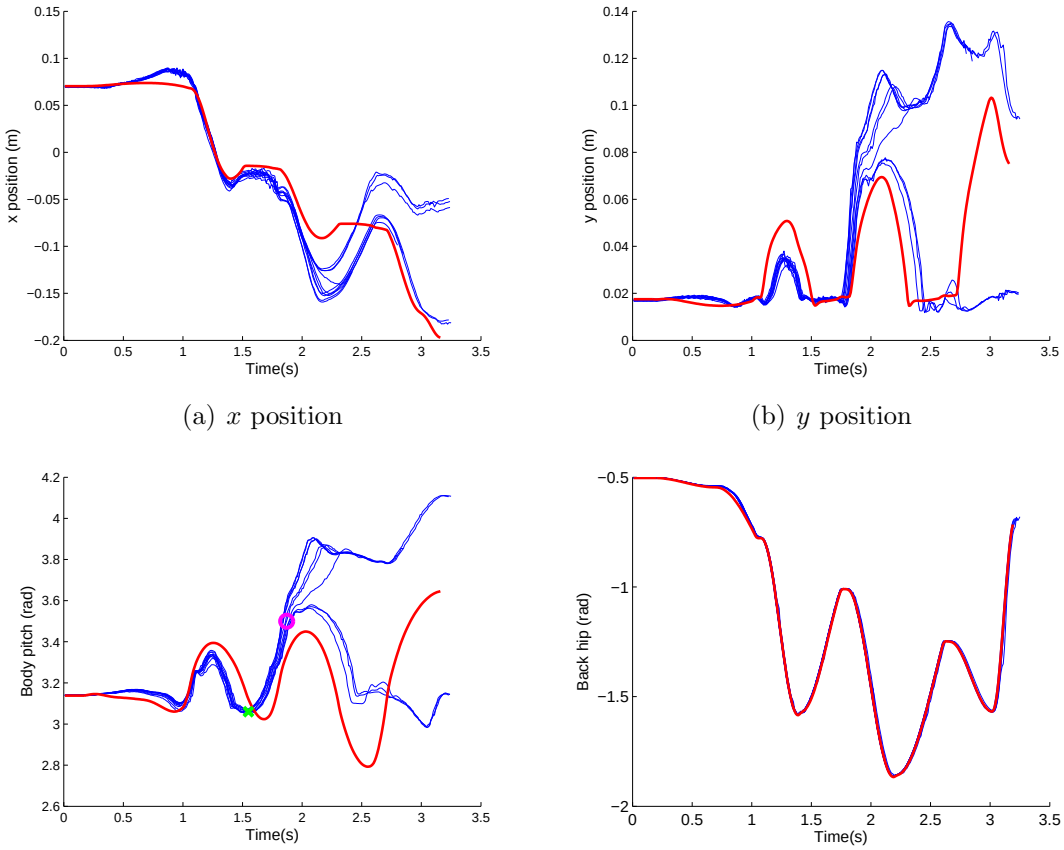

(a) x position

(b) y position

(c) Body pitch

(d) Back hip joint position

Figure 3-5: Model repeatability

The unactuated coordinates for a bounding motion (x, y, and body pitch) and a trajectory of one of the joints. The thick red line shows a trajectory generated by planning with RRT's using the simulation model. The thin blue lines are 10 open-loop runs of the same trajectory on a real LittleDog robot. In (c), the 'x' shows where trajectories begin to separate, and the 'o' show where trajectories finish separating.

Symbol	Value	Units	Description
Rigid-body model			
Shin			
m_1	0.13	kg	Mass of shin
l_1	9.2	cm	Length of shin
I_1	7×10^{-5}	$kg\ m^2$	Inertia of shin
cx_1	5.7	cm	Center of mass in x for shin
cy_1	0.3	cm	Center of mass in y for shin
Upper leg			
m_2	0.24	kg	Mass of upper leg
l_2	7.5	cm	Length of upper leg
I_2	6×10^{-6}	$kg\ m^2$	Inertia of upper leg
cx_2	4.8	cm	Center of mass in x for upper leg
cy_2	-0.9	cm	Center of mass in y for upper leg
Main body			
m_3	2.3	kg	Mass of body
l_3	20.2	cm	Length of body
I_3	2.2×10^{-3}	$kg\ m^2$	Inertia of body
cx_3	8.7	cm	Center of mass in x for body
cy_3	-0.2	cm	Center of mass in y for body
Motor model			
Hip joint			
k_{hip}	3800	$1/s^2$	Hip gain
b_{hip}	98	$1/s$	Hip damping
$\bar{v}_{hip}$	7.9	rad/s	Hip velocity saturation
$\bar{a}_{hip}$	200	rad/s^2	Hip acceleration saturation
Knee joint			
k_{knee}	9700	$1/s^2$	Knee gain
b_{knee}	148	$1/s$	Knee damping
$\bar{v}_{knee}$	12	rad/s	Knee velocity saturation
$\bar{a}_{knee}$	430	rad/s^2	Knee acceleration saturation
Ground contact model			
Friction			
K_f	0.5	$none$	Friction gain
K_d	1000	s/m	Friction velocity slope
Normal spring			
K_h	1.4×10^5	N/m	Ground stiffness
ζ_h	1.4	s/m	Ground damping
Shin spring			
K_s	7500	N/m	Spring linear stiffness
b_s	180	Ns/m	Spring linear damping
K_c	7500	N/m	Spring limit stiffness
ζ_l	180	s/m	Spring limit damping
l_{max}	0.88	cm	Maximum spring travel (spring limit)
β	0.29	rad	Angle between spring and shin joint
r_b	1.0	cm	Foot radius

Table 3.1: LittleDog model parameters

Chapter 4

State Estimation

The purpose of the state estimation algorithm is to use the available sensors to create an accurate estimate of LittleDog's state, with the goal of making the combination of the estimator and the robot behave similarly to the idealized model developed in Chapter 3. This involves using the robot's model to eliminate the noise in the sensors, compensate for sensor delays, and estimate states that are not instantaneously observable and need to be derived from sensor readings across multiple time steps. An accurate estimate of the current state allows the use of full state feedback in the controller.

4.1 LittleDog Sensor and Control Environment

As shown in Figure 4-1, the LittleDog robot is equipped with a number of sensors to help estimate the state of the robot. The joints contain encoders mounted on the shafts of the motors, giving a low-noise reading of the motor positions, but making any effects of backlash unobservable. An on-board IMU (Inertial Measurement Unit) uses a set of gyroscopes and accelerometers to measure linear accelerations and rotational velocity of the robot. A set of reflective markers secured on the outside of the robot's shell allows a motion capture (MOCAP) system to measure the position of the robot.

In addition to these, LittleDog's feet are equipped with a set of force sensors, but we opted to not use them in our state estimation approach. These sensors could be

used to detect collisions with the ground, but we found that in order to make the detection reliable we had to set a high threshold, which delays the contact detection. Detecting collisions by monitoring state estimates is simpler and has worked sufficiently well in this case. Further work in improving the estimator could look into incorporating force measurements to create better estimates in the region of transitions to and from ground contact and to better detect transitions between modes, describes later in the text.

The time delay in reading the encoders is limited to communication delays and is small with respect to the 10ms timestep, so the encoders are assumed to have 0 delay for the purposes of state estimation. Experiments on the robot show that the IMU has a delay of about 3 time steps, possibly because of low-level filtering in the sensor. The MOCAP data also shows a delay of approximately 3 time steps, which arises because of time needed to process the image data and calculate the coordinates of the reflective markers.

As mentioned in Chapter 3, each of the motors at the joints is controlled by a servo loop located on board of LittleDog and executed at 500Hz. The gains for the servo controllers are fixed and the velocity set points are fixed at 0, while the position set points act as the control inputs for the off-board control algorithm and are referred to as control inputs or motor commands in this work. The external, or off-board, control loop is executed at a frequency of a 100Hz and communicates to the robot over IP, using the Lightweight Communications and Marshalling (LCM) library[15]. The loop is shown in Figure 2-1 in red and the design of its estimation and control components is the focus of this work, with other elements such as the model supporting this goal.

Every 10ms, the external control loop gets the latest readings from the encoders and the IMU on board of the robot, and the MOCAP system off-board. The estimator uses the new data to update the current state estimate of LittleDog and passes it to the feedback control algorithm, which then computes a set of motor commands that are to be sent to the robot. After transmitting the commands to the servo loop, the external loop goes idle until the next time step. The execution time of the estimation and control step, including the time spent on communication, adds a small delay to

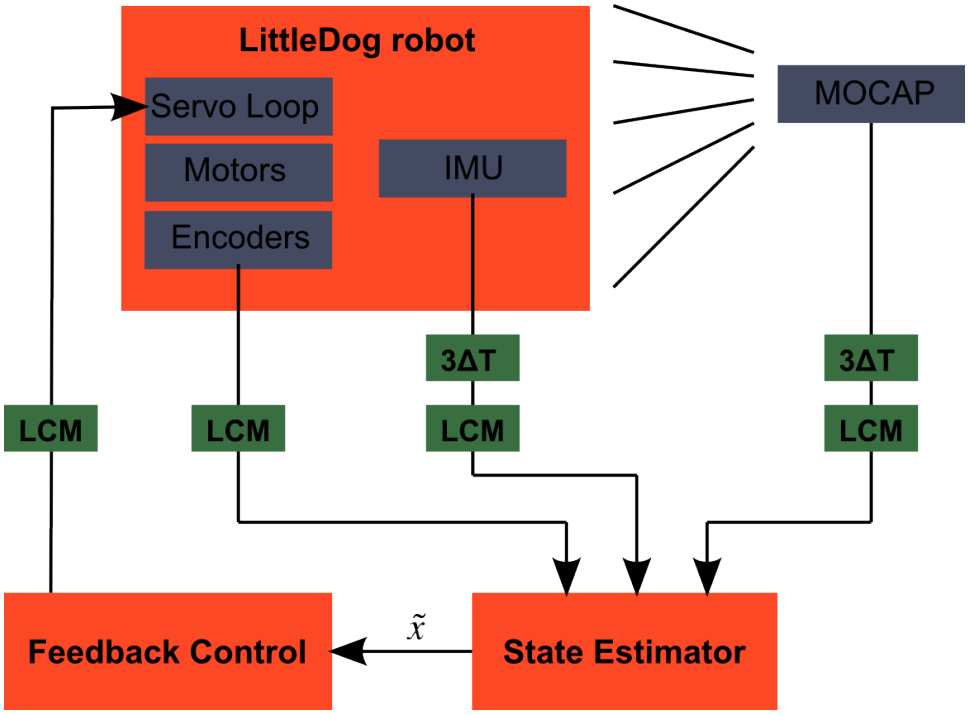

Figure 4-1: LittleDog sensing and control environment
LittleDog is equipped with an encoder on each motor, an Inertial Measurement Unit, a set of markers to be used in a MOtion CAPture environment, and force sensors, with the latter not being used in this work. The IMU data is delayed by 3 time steps because of internal filtering, while MOCAP is delayed by 3 time steps because of processing to extract marker position from images. We use the LCM library [15] for communication between all of the elements.

the system, as the motor commands become slightly outdated by the time they arrive at the motors.

4.2 Extended Kalman Filter with Time Delays

The classical version of the Extended Kalman Filter (see [5]) either doesn't explicitly account for delays or assumes an equal known delay for all sensors, but can be naturally augmented to incorporate them into the algorithm. In the case of LittleDog, the encoder readings are current, while the IMU and MOCAP data is assumed to be delayed because of filtering and computational delays. The problem of delays in estimation data has been studied by a number of authors ([40],[49],[27]). In particular, the minimum variance estimation problem for a linear system with variable delays

for each sensor (with the potential of data loss) has been previously solved, and the estimator has been demonstrated to be exponentially stable [27]. In this section we discuss our implementation of the Extended Kalman Filter with time asynchronous time delays, which can be thought of as a specific case of that problem on the linearization of the system.

Consider a system with discrete dynamics given by

$$x[n+1] = f(x[n], u[n]) + w[n],$$

where $x[n]$ is the system state at time step n, $u[n]$ is the control input at the time step, and $w[n]$ is zero mean Gaussian random noise given by

$$\mathbf{E}[w[n]w[l]^\top] = Q[n]\delta(n,l),$$

where $\delta(n,l)$ is the Dirac delta function, and $Q[n] \geq 0$ is its covariance. The system has a set of M sensors described by

$$z_k[n] = h_k(x[n-\rho_k]) + v_k[n], k \in [1,\ldots,M],$$

where $z_k[n]$ is the k'th sensor reading, delayed by $\rho_k \in \mathbb{N}_0$ time steps, and $v_k[n]$ is zero mean Gaussian random noise such that

$$\begin{aligned}
&\mathbf{E}\{v_k[n]v_k[l]^\top\} = R_k[n]\delta(n,l),\\
&\mathbf{E}\{v_k[n]v_m[l]^\top\} = 0 \text{ for } k \neq m, \forall n, l,\\
&\mathbf{E}\{v_k[n]w_m[l]^\top\} = 0 \text{ for } \forall k, l, m, n,\\
&R_k[n] > 0.
\end{aligned}$$

In addition, an estimate of the initial state $\tilde{x}[0] = \mathbf{E}\{x[0]\}$ and its covariance $P[0] = \mathbf{E}\{(x[0]-\tilde{x}[0])(x[0]-\tilde{x}[0])^\top\}$ are available. For consistency, assume that $z_k[n]$ is zero for $n \leq \rho_k$. Let $\rho_{max} = \max_k \rho_k$. Let $\tilde{x}[l,n]$ and $P[l,n]$ represent the minimum variance estimate of $x[l]$ and its covariance based on the sensor measurements up to

timestep n, i.e. $\{z_k[m] \mid k \in [1,\ldots,M], m \in [1,\ldots,n]\}$. The goal of the estimator is to compute $\tilde{x}[n,n]$ for each time step n. Note, that when $\rho_k = 0, \forall k$, the framework is identical to that of the standard discrete-time Extended Kalman Filter.

The vector of all of the sensor measurements generated by state $x[l]$ and available at time step n is

$$Z[l,n] = \{z_k[l+\rho_k] \mid l+\rho_k \leq n, k \in [1,\ldots,M]\}. \tag{4.0}$$

For $\rho_k \geq 0$ and $l > n$, $Z[l,n] = \emptyset$, as expected, since sensor measurements from future states are not available. Also, after a sufficient time, no new information is received about the old states, so

$$\left.\begin{aligned} Z[l,n] &= Z[l,m] \\ \tilde{x}[l,n] &= \tilde{x}[l,m] \\ P[l,n] &= P[l,m] \end{aligned}\right\} \forall n, m \geq l + \rho_{max}. \tag{4.0}$$

Just as in the regular Extended Kalman filter, the estimates are computed online and recursively. For iteration n the vectors $\{Z[l,n], l \in [n-\rho_{max},\ldots,n]\}$ are computed using the new sensor readings $\{z_k[n], k \in [1,\ldots,m]\}$ according to (4.2). Given previously computed $P[n-1-\rho_{max}, n-1] = P[n-1-\rho_{max}, n]$ and $\tilde{x}[n-1-\rho_{max}, n-1] = \tilde{x}[n-1-\rho_{max}, n]$ (where the equality follows from (4.2)), one can get the current state estimate, $\tilde{x}[n,n]$, by recursively applying the prediction and update steps of the Kalman filter for $m \in [n-\rho_{max},\ldots,n]$:

$$\begin{aligned} \tilde{x}^*[m,n] &= f(\tilde{x}[m-1,n], u[m-1]) \\ P^*[m,n] &= F_{m-1,n} P[m-1,n] F_{m-1,n}^\top + Q[m-1] \\ S[m,n] &= G_{m,n} P^*[m,n] G_{m,n}^\top + \mathcal{R}[m] \\ K[m,n] &= P^*[m,n] G_{m,n}^\top S^{-1}[m,n] \\ \tilde{x}[m,n] &= \tilde{x}^*[m,n] K[m,n](Z[m,n] - H[m,n]) \\ P[m,n] &= (I - K[m,n] G_{m,n}) P^*[m,n], \end{aligned}$$

where

$$
\begin{aligned}
F_{l,n} &= \frac{\partial f}{\partial x}(\tilde{x}[l,n]) \\
H_{l,n} &= \{h_k(\tilde{x}[l,n]) \mid l + \rho_k \leq n, k \in [1,\ldots,M]\} \\
G_{l,n} &= \left\{ \frac{\partial h_k}{\partial x}(\tilde{x}[l,n]) \mid l + \rho_k \leq n, k \in [1,\ldots,M] \right\},
\end{aligned}
$$

with the vector $H_{l,n}$ and matrix $G_{l,n}$ having the same ordering as $Z[l,n]$, and with $\mathcal{R}[m]$ constructed in a similar way by stacking matrices $R_k[m]$ as blocks on the diagonal. For the first few iterations while the filter initializes, when $n \leq \rho_{max}$, the computations are done for $m \in [1,\ldots,n]$.

Evaluating (4.2) produces the desired estimate $\tilde{x}[n,n]$, as well as $\tilde{x}[n-\rho_{max},n]$ and $P[n-\rho_{max},n]$, which are needed for the next time step of the filter. For LittleDog, the prediction step (first line in (4.2)) is run for an extra iteration using an estimate of $u[n]$ to get $x[n+1,n]$, which is sent as the current state to the controller. The slight feedforward in estimation helps to compensate for delay in command execution on the robot.

4.3 Modified Dynamics Model

As described in Chapter 3, the dynamical model of LittleDog has a total of 16 states, 2 of which describe the first-order spring dynamics in the feet of the robot and are primarily involved in ground interaction modeling. The pair of springs has stiff dynamics, significantly faster than the control and sensing rates of the robot, and are heavily coupled to other states, such as the body position.

Because of difficulty in estimating the spring states and high sensitivity of the dynamics to their errors, it is best to eliminate the two states from the estimation and control loop. This is accomplished by using a pinned version of the model for the estimation and by not using the spring states for feedback.

Using a pinned version makes it necessary to construct 3 separate versions of the model, corresponding to different modes of the dynamics: pinned at the back foot,

pinned at the front foot, and in double support. To construct the version of the model pinned at the back foot, the ground contact part of the LittleDog model from Chapter 3 is discarded, while keeping the rigid body and motor components and constraining the back foot to remain fixed in space. This ignores foot roll, foot slip and changes in leg length due to leg spring compression, first two of which should be small for well-designed bounding trajectories. The positions of the motors at the joints are still computed exactly as in the full model, while the body pitch dynamics are slightly different. An equivalent construction is used for the version of the model pinned at the front foot.

For the double support mode, both feet are constrained to be at the ground and both the ground contact and rigid body dynamics portions of the model are discarded, only simulating the joint dynamics. The motion of the robot body is computed to keep the feet of the robot on the ground and minimize their motion along it.

The simplified models are used to compute the prediction term and the model gradients in (4.2). The estimator keeps track of the current mode of the dynamics and switches between different versions of the simplified model, as necessary. Because of the simplifications, this version is less accurate than the full model, but it is not a problem for the estimator, because only a few time steps of prediction are necessary and the sensor data provides feedback to guide the estimates. As described later in this work, the control is applied only during single support modes, so it is more important to have good state estimates during those parts of the trajectory. For that reason, both the system identification and the state estimation focus on accuracy during the single support phase. The highest errors in state estimation occur after the collision (transition into double support), in the double support mode itself, and less so after transition out of double support. However, the dynamics in double support are stable and any errors remaining after transitioning into single support dissipate quickly.

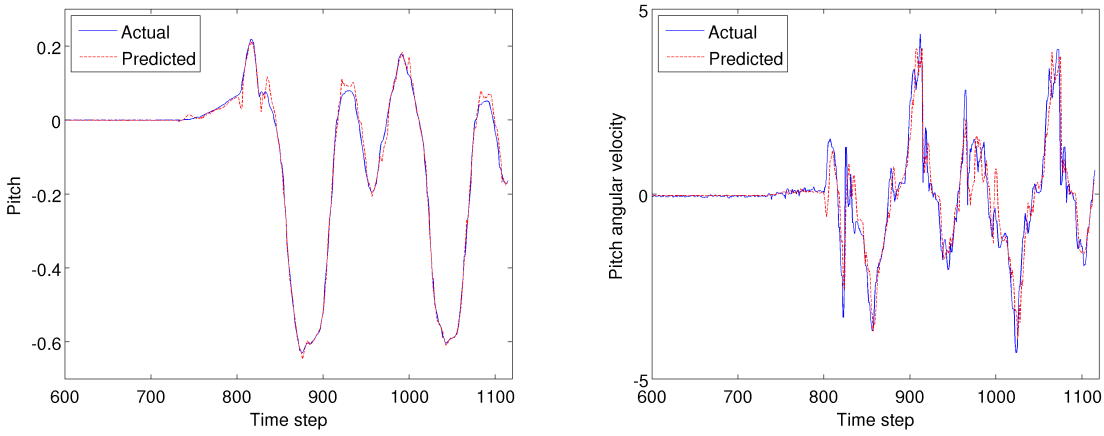

Figure 4-2: Estimator performance on real data
System states predicted by the estimator versus actual values computed from non-casual filtering. Pitch, shown in the left plot, is from MOCAP data, while pitch derivative, shown in the right plot, is from IMU data.

4.4 Estimator Performance

The estimator parameters were fit to real data collected from the robot's sensors against the best non-causal estimate of the system's state. The $\{\rho_k\}$ described in section 4.2 were set to 3, 3, and 0 for MOCAP, IMU, and encoders, respectively, to compensate for the delays in these sensors. Because, unless the current estimate is extremely poor, the estimator error dynamics are stable, it is more difficult to evaluate its performance than that of a dynamics model or a controller. A good estimator will not have a significant lead or lag, will not damp out significant dynamics in the system, while introducing as little of its own dynamics as possible to the closed loop system. We fit the estimator parameters by minimizing the weighted sum of squared errors over all of the sensors.

Figure 4-2 shows example fits for LittleDog body pitch (on the left) and its angular velocity (on the right). As seen in the figure, there are errors in the estimates, but both the position and velocity follow the nominal closely and there is little to no lead or lag.

Chapter 5

Feedback Control

As discussed in Chapter 2, our approach to bounding control is divided into trajectory planning, state estimation, and trajectory stabilization parts. Chapter 3 discusses the dynamical model that makes all 3 of the components possible, and Chapter 4 explains the estimation algorithm that provides the current state estimate. This Chapter discusses the design and implementation of the feedback control algorithm that uses the current state estimate to stabilize the planned trajectories.

5.1 Transverse Linearization

5.1.1 Transverse Linearization on Continuous Systems

Classical control techniques, as well as many of the more modern methods, such as H-infinity [32] and the Linear Quadratic Regulator (LQR), focus on controlling a given system to a fixed equilibrium state. By making the equilibrium position time-varying some of them can be extended to stabilize a trajectory. This can work well when there are large amounts of actuation available and there is good controllability, but could produce strange results such as moving the system away from the goal if the system reaches it too early. When the system is underactuated, this approach, in general, requires large control efforts and can result in poor performance. For example, attempts to design a time-varying LQR controller on the linearization of the

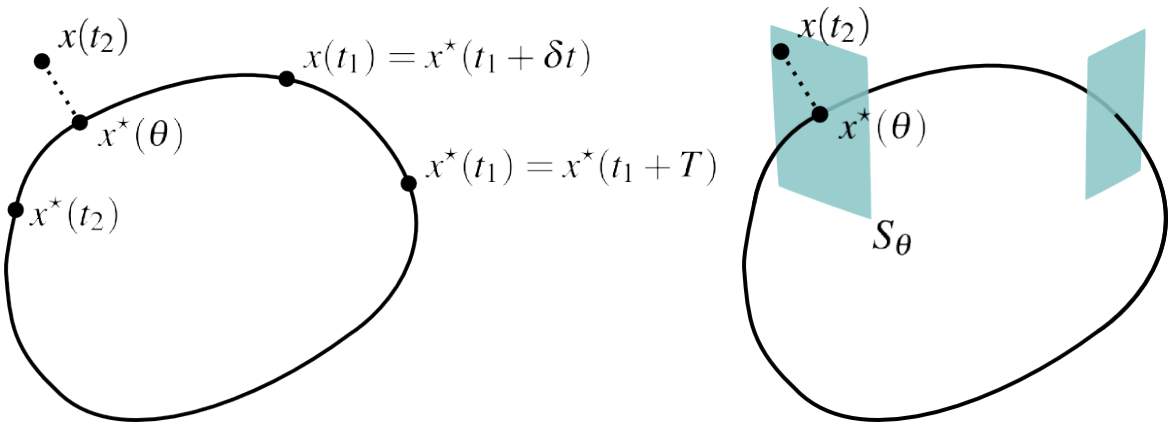

Figure 5-1: Transverse coordinates for orbits in state space
On the left plot, if the goal is to stay on the nominal orbit and a system gets ahead in time to state $x(t_1)$ instead of $x^\star(t_1)$, a time-based controller will try to correct this error, unnecessarily. Instead, it makes sense to minimize the error to the closest nominal point, which is defined in the right plot by constructing a set of transverse surfaces that map an arbitrary state back to the nominal orbit.

LittleDog model around a trajectory of a single bound were not successful, because the controllability matrix was poorly conditioned, which made it numerically impossible to solve the Riccati equation.

When the time to get to the goal is irrelevant, it should be possible to do better by not enforcing a particular time for each point on the trajectory. To illustrate this, consider stabilizing a system to an unstable orbit (a closed unstable periodic trajectory) with states $x^\star(t) = x^\star(t + T)$ and actions $u^\star(t) = u^\star(t + T)$ (see figure 5-1, left). Let point $x = x^\star(t_1 + \delta t)$ in the figure be the current state of the system and $x^\star(t_1)$ be the position on the original orbit at current time. Since x is already on the trajectory, it is possible to remain on it by applying the command $u^\star(t_1 + \delta t)$ instead of $u^\star(t_1)$. A controller that relies on time for knowing the system's position on the trajectory will see an error of $x^\star(t_1) - x^\star(t_1 + \delta t)$ and attempt to correct x towards $x^\star(t_1)$ as well as using $u^\star(t_1)$ for the feedforward term, when $u^\star(t_1 + \delta t)$ would be more appropriate. This might result in unnecessary and large control efforts, the latter being especially true for underactuated systems.

A known solution for this is to parametrize the trajectory and make the controller depend on this parameter instead of time [13]. Let $\theta \in [0, T)$, referred to as phase

in this work, be this parameter defined such that $x^\star(\theta) = x^\star(t), \forall\theta$. Because, as mentioned, the real system is not expected to perfectly remain on the theoretical trajectory, to make the phase useful in practice it is important to extend it to the state space beyond the original orbit. This can be done in more than one way and a number of approaches have been previously used.

A general way of extending phase to a wider region of state space is to define a set of surfaces of equal phase corresponding to each point on the orbit (see figure 5-1, right, for illustration). These surfaces are constructed in such a way that at every point on the orbit the dynamics have a component orthogonal to the corresponding surface. We will refer to the region of state space where these surfaces are well-defined as the region of validity of the transformation, and their collection forms a set of θ-parametrized Poincare sections for all of the points on the orbit:

$$S_\theta = \{x : \theta(x) = \theta, x \in \Omega\},$$

where $\theta(x)$ is a function that computes the phase for a state inside the region of validity, Ω. Orbital stability can be thought of as a stable return map of the dynamics on these sections. For an M-dimensional state space, a set of $M-1$ coordinates describing the position on a given S_θ are known as the transverse coordinates, and the transverse surfaces define, within the region of validity, a coordinate transformation from the original state space to a new one consisting of the phase and the transverse coordinates.

For a given point in state space, the component of the system's dynamics along the corresponding surface are the transverse dynamics of the system. A controller designed to stabilize the transverse dynamics, but not regulating the value of phase, will achieve the goal of orbital stability, while typically requiring significantly less control effort than a time-referenced controller, because it is regulating fewer state variables. The method of transverse linearization accomplishes this by linearizing the dynamics at every point along the orbit so that linear control techniques can be used to achieve orbital stability. The method of transverse coordinates can be applied

to non-periodic, finite trajectories by substituting the task of stability by that of minimizing a cost function and adopting the convention that trajectories terminate when they reach the phase of the goal state. This work uses phase-based finite-horizon LQR applied to the transverse linearization of the LittleDog dynamics.

As mentioned, the definition of the transverse surfaces and the process of linearization limit the region in which the controller is effective. Appendix A describes our work on deriving guaranteed regions of stability of a transverse controller on a simple periodic walking system.

5.1.2 Orthogonal Surfaces

The use of transverse linearization in this work requires a robust and easily computable way of constructing the transverse surfaces for arbitrary planned trajectories. This can be done by defining the surface at phase θ, S_θ, as a hyperplane orthogonal to the trajectory at $x^\star(\theta)$ with respect to some distance metric d. Then, the phase for a state sufficiently close to the trajectory can be computed as

$$\theta(x) = \arg\min_{\tau} \|x^\star(\tau) - x\|_d. \tag{5.0}$$

For a differentiable trajectory this is always well defined locally. The connected region of state space that includes the trajectory where the minimum is unique is the region of validity of this definition and depends on the distance metric as well as on the shape of the trajectory.

This work defines the distance metric in terms of Euclidean distance by choosing a positive definite matrix W:

$$\|z\|_d = \|\sqrt{W}z\|. \tag{5.0}$$

There is a compelling argument for making W varying with the phase along the trajectory to increase the region of validity and optimize other properties of the surfaces, but it is kept constant in this work for simplicity.

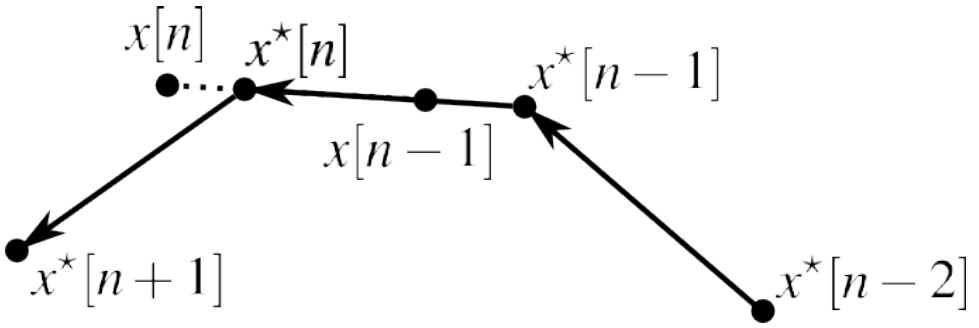

Figure 5-2: State space trajectory of a system with discrete-time inputs
For a system with a continuous state space, but control inputs discretized in time, a control input that works at timestep $n-1$ might not be as good half a timestep later, making the notion of a nominal control input outside of the nodes hard to define. When trying to apply the method of transverse coordinates, this requires careful consideration of projection surfaces, phase calculation, and a new concept of orbital stability.

5.1.3 Discrete Approximation

Implementation on a real system usually requires a controller to be converted into discrete form. If the time interval between adjacent control actions is small in comparison to the timescale of the system's dynamics, this tends to not be a problem because there is little difference between the continuous control input and a discretized signal. However, when the time step is relatively large, the commands might be changing significantly between two adjacent time steps. For LittleDog, a full bounding motion, which is the length of time from the moment that a set of legs touches down, lifts off, and touches down again, might take as little as 50 time steps, only 0.5s. The time constants of the collision and joint dynamics are significantly faster than the 0.01s control steps, while the body pitch dynamics can have a time constant of as little as 0.1s. Because of that, even though the underlying system is continuous, the model developed in section 3 and used in control design is discrete, obtained by integrating a continuous physics model for 0.01s with a zero-order hold on the control input. In this case the discretization effects are significant, so, unlike previous implementation of transverse linearization, the effect of discrete dynamics is explicitly considered when stabilizing LittleDog bounding.

Consider a trajectory of length N for a discrete-time system with dynamics

$$x[n+1] = f(x[n], u[n])$$

and timestep δt, represented by states $x[0], \ldots, x[N]$ and corresponding control commands $u[0], \ldots, u[N-1]$. Defining the phase as a discrete variable loses information about the state, resulting in up to 1 timestep of error in the control command and could add significant discretization errors. This could be a big issue when the timestep is relatively large and there is a strong feedforward term, as in the case of LittleDog. In this case, it is possible to think of the discrete dynamics as an integral over the continuous dynamics with a continuum of states along the whole trajectory. A continuous trajectory has the benefit of allowing one to define a continuous phase variable to index into the trajectory, but creates a number of issues as illustrated in Figure 5-2. First of all, because the control input changes discontinuously between the timesteps, the derivative of the trajectory is not defined at those times. Therefore, if the transverse surfaces are constructed according to (5.1.2), they are not defined at those points and have small regions of validity in the vicinity. Secondly, even if the transverse coordinates are zero at a point on the trajectory, applying the nominal control input will not in general make the system remain on the nominal trajectory. To deal with both of these problems, we interpolate between adjacent timesteps for the purposes of constructing the transverse surfaces and applying control, as well as making a number of other approximations.

5.2 Implementation for Control of LittleDog

5.2.1 Phase Variable Selection

Using (5.1.2) to compute the current phase for a point in state space depends on the choice of W and the method of interpolation for adjacent points on the discrete trajectory (referred to as nodes when describing them as part of the continuous trajectory). To be as effective as possible, the phase computation should be robust to

noise in the state estimates and to errors in the model dynamics and give reasonable result when the system has large deviations from the nominal trajectory.

Previous studies used one of the kinematic states of the system to determine the current phase of a robot ([24],[52]). This has the benefit of the phase being independent from most other variables, separating the states involved in computing the phase and states that need to be actively controlled, and it is generally easy to compute. However, this approach is not possible on a robot such as LittleDog, where within any particular bounding trajectory, none of the angles of the robot increase or decrease monotonically, and the robot's configuration might repeat within a given trajectory. Therefore, a balance between the weights on position and velocity states is desired for the purpose of phase computation.

We refer to the angle formed between the vertical and the line from the supporting foot to the center of mass of the robot as the LittleDog pendulum angle or the center of mass (COM) angle. To first approximation, the dynamics of LittleDog during a bounding motion is that of a simple pendulum, so we also refer to the COM angle dynamics as the LittleDog pendulum dynamics. The motions of the legs and the body can be effectively thought of as an inertial wheel with varying inertia and as changing the length of the pendulum, and these motions have a large effect on the dynamics. However, except for near the unstable equilibrium, the COM component of the dynamics dominate the overall direction during a trajectory. Furthermore, unlike the position of the joints, which can be easily set to the desired position, the COM dynamics capture the underactuated nature of the bounding robot, so it is natural to make the phase computation heavily rely on these states.

Neither the COM angle nor the COM angular velocity are, in general, monotonic during LittleDog bounding trajectories, but there is a unique pair of these two variables for each point in all of our bounding trajectories. The COM velocity goes to zero at certain points in all of the bounding trajectories that we used, so it was impossible to rely on the COM angle for phase estimation. However, the estimates of COM velocity are noisier, which prevents one from heavily relying on them, as well.

As was discussed in Chapter 3 and can be seen in Figure 3-1, the state of LittleDog

is described by the body position, the angles of the joints, the pitch, the derivatives of all these, as well as the positions of the ground contact springs. Using the COM angle instead of pitch still allows a full description of the state space. Let $\mathcal{G}$ be a map from the state space using the pitch angle and pitch velocity to that using the COM angle and COM velocity. Both state descriptions are complete, so the map is invertible. Given a segment $(x^\star[0], \ldots, x^\star[n])$ of a discrete trajectory and a current state estimate x, we compute distances from x to all points on the trajectory, $(r_0, \ldots, r_n)$, as

$$r_i = \|\sqrt{W}(\mathcal{G}(x) - \mathcal{G}(x^\star[i]))\|,$$

with W heavily weighted towards the COM angle and COM angular velocity and, although not necessary for this method, diagonal for simplicity. To approximately find the phase of the closest point on the trajectory, we compute the minimum of a parabola fit through the 3 lowest values of r_i. This is an approximate method to get $\theta(x)$, but in practice we found it to be the most robust to errors in estimation and model errors.

5.2.2 Effect of Collisions

As described in section 4.3, planned LittleDog trajectories are divided into segments based on the mode of the dynamics: pendulum mode on back leg, pendulum mode on front leg, and double support mode. Starting from a planned trajectory and a terrain map, the division into segments and classification is done by thresholding on the height of the back and front feet above the terrain. Figure 5-3 shows an example classification, with red and blue showing the height of the back and front feet, respectively, and asterisks showing the borders between the segments. The double support phase is intentionally made larger, to be conservative. Note, that it is important to accurately detect mode transitions, as transitioning too early or too late may result in having a state far away from the nominal trajectory or outside the region of validity, potentially resulting in unexpected collisions or divergence from the nominal trajectory.

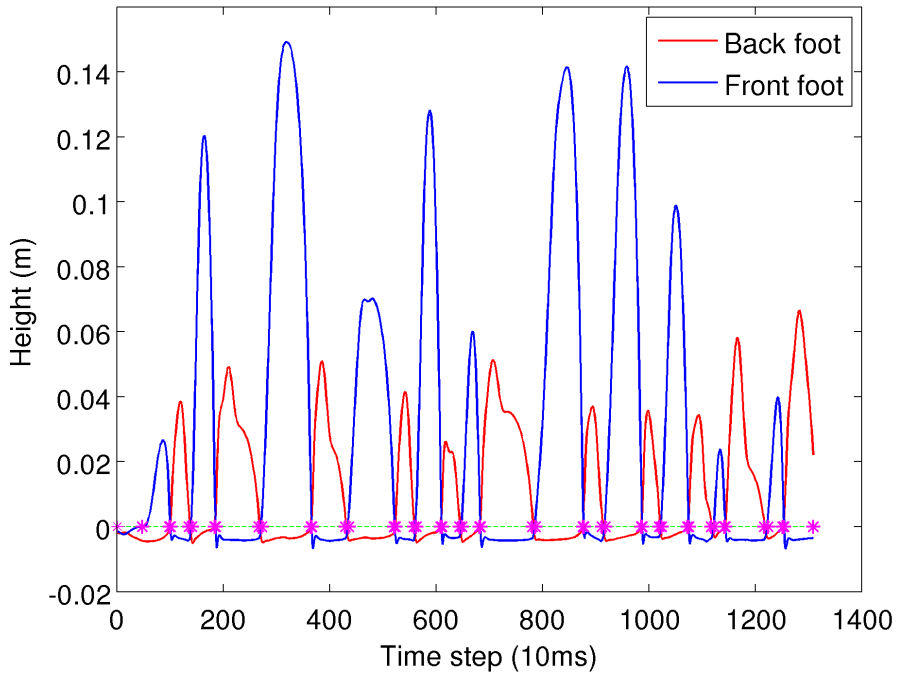

Figure 5-3: Partition of a trajectory into segments by dynamics mode
The method used to divide the bounding trajectory into segments for the 3 dynamics modes: on back feet, on front feet, and in double support. The partition is based on the height above the terrain map of the front and back feet in simulation, shown in the plot. The lines go below 0, shown by the green line, because this doesn't account for leg springs, and the collision model allows for small amounts of ground penetration. Magenta asterisks show the locations of mode transitions. After the partition, the double support segments are slightly expanded to introduce an error margin.

Each segment is treated as a separate control problem for the purposes of phase computation and stabilization of transverse coordinates. The current phase is computed only by considering the pieces of the trajectory in the current segment and, when the current phase reaches the end of the segment, the system is assumed to transition into the next mode. There is some overlap between the segments to smooth out the transition. For transverse coordinate stabilization design, the final state is the last nominal state in a segment.

The dynamics are stiff near the collisions, so small errors in state estimation or small model errors might have a large effect on the control input. Because of this and time delays, it becomes difficult to have beneficial feedback control near the collisions, so our controller doesn't stabilize transverse coordinates during the double support mode (which is, essentially, a continuous collision) and a few time steps prior to the expected collision, to account for potential model or state estimation errors. Luckily, ground interactions are stabilizing for pitch in double support mode, so it is not as necessary to have good feedback during this mode.

5.2.3 LQR in Transverse Coordinates

For each segment of the trajectory that is in pendulum mode of the dynamics, the commands computed by the RG-RRT planner are augmented by feedback from an optimal linear controller designed on the linearized transverse dynamics of the system. The gains for each time step of the segment are computed offline and are then interpolated based on the current phase during the execution. Note that there is no need to smooth the commands coming out of RG-RRT, because of its use of smooth half-bound motion primitives [46].

Let $x[n+1] = f(x[n], u[n])$ represent the pinned (without ground model) dynamic model of LittleDog for one of the pendulum modes. Let $(x^\star[0], \ldots, x^\star[N])$ be a segment of the nominal trajectory with all points in the same dynamics mode and $(u^\star[0], \ldots, u^\star[N-1])$ be the corresponding nominal control input. The surface

normals $(z[1], \ldots, z[n-1])$ are computed as

$$z[n] = \frac{W(\mathcal{G}(x[n+1]) - \mathcal{G}(x[n-1]))}{\|W(\mathcal{G}(x[n+1]) - \mathcal{G}(x[n-1]))\|},$$

with $z[0]$ and $z[n]$ approximated using a one-sided difference. A 15×16 matrix Π_i of unit vectors representing the transverse coordinates is computed for each time step from the z's and a random vector w_{ref} using the algorithm in [23], so that $\Pi_n^\top \Pi_n = I$, $\Pi_n \Pi_n^\top = I$, and $\Pi_n z[n] = 0$.

Computing the linearized transverse dynamics gives

$$\begin{aligned}
\tilde{A_n}' =& \Pi_{n+1} W \left.\frac{\partial \mathcal{G}}{\partial x}\right|_{x[n+1]} \left.\frac{\partial f}{\partial x}\right|_{x[n],u[n]} \left.\frac{\partial \mathcal{G}}{\partial x}^\top\right|_{x[n]} W^{-1} \Pi_n^\top \\
\tilde{B_n} =& \Pi_{n+1} W \left.\frac{\partial \mathcal{G}}{\partial x}\right|_{x[n+1]} \left.\frac{\partial f}{\partial u}\right|_{x[n],u[n]} \\
\tilde{A_n} =& c2d\left[d2c\left(\tilde{A_n}'\right) - \frac{\Pi_{n+1}\Pi_n^\top + \Pi_n \Pi_{n+1}}{2\Delta t}\right],
\end{aligned}$$

where the last line is an approximation to correct for the rotation of the coordinate system with time, $c2d$ converts a discrete dynamical system to its continuous analog and $d2c$ does the converse. On the linearized dynamics $\tilde{A}, \tilde{B}$ for each segment we then design the gains using the Riccati equation for a finite LQR controller:

$$\begin{aligned}
P_n =& \tilde{A}_n^\top (P_{n+1} - P_{n+1}\tilde{B}_n(\tilde{B}_n^\top P_{n+1}\tilde{B}_n + \tilde{R})^{-1}\tilde{B}_n^\top P_{n+1})\tilde{A}_n + \tilde{Q}_n \\
\tilde{K}_n =& (\tilde{B}_n^\top P_{n+1}\tilde{B}_n + \tilde{R})^{-1}(\tilde{B}_n^\top P_{n+1}\tilde{A}_n),
\end{aligned}$$

where the cost matrices are computed as

$$\begin{aligned}
P_{N+1} =& \Pi_{N+1} W^{-\top} Q_f W^{-1} \Pi_{N+1} \\
\tilde{Q}_n =& \Pi_n W^{-\top} Q W^{-1} \Pi_n \\
\tilde{R}_n =& \Pi_n W^{-\top} R W^{-1} \Pi_n
\end{aligned}$$

and the cost matrices Q,Q_f,and R are chosen in the COM coordinates, heavily weighted toward the COM angle and COM angular velocity. Finally, the gain matri-

ces are converted from transverse to COM coordinates:

$$K_n = \tilde{K}_n \Pi_n W.$$

During runtime, given the current state x, the current phase $\theta(x)$ is computed as described in section 5.2.1. Then, for n such that $n \leq \theta < n+1$, K_θ is computed by cubic spline interpolation from the pair $\{K_n, K_{n+1}\}$, $x^\star_\theta$ and $u^\star_\theta$ are both computed by cubic interpolation from $\{x^\star[n], x^\star[n+1]\}$, and $\{u^\star[n], u^\star[n+1]\}$, respectively. The controller produces the motor command given by

$$u = K_\theta(\mathcal{G}(x^\star_\theta) - \mathcal{G}(x)) + u^\star_\theta.$$

Figure 5-4 shows an example of a stabilized segment of a bounding trajectory on flat with small process noise and small estimation errors. The trajectory starts at the top and moves towards the bottom of the figure. The asterisks mark the projection of the states at each time step onto the COM angle and COM angular velocity plane, forming the trajectories as seen in the figure. At each time step, they are also projected on the nominal trajectory to compute the current phase.

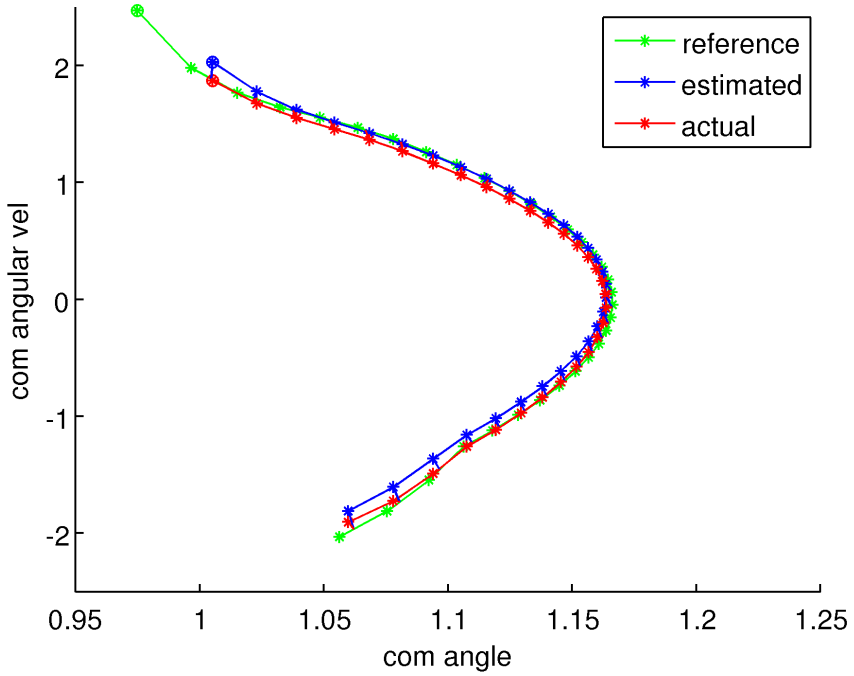

Figure 5-4: Example of stabilized trajectory segment
Plot of a bounding trajectory segment in the COM angle and COM angular velocity plane, which are the main components of phase calculation, in a low process and sensing noise environment, with no delays. The estimated trajectory is the one available to the feedback controller.

Chapter 6

Results

6.1 Simulation Results

6.1.1 With Perfect State Knowledge

We have simulated the transverse-linearization controller with a number of RRT-generated bounding trajectories. For some trajectories over flat terrain in simulation, we were able to achieve stable bounding even when adding a combination of: 1) slight Gaussian noise to the state estimate ($\sigma = 0.01$ for angles, $\sigma = 0.08$ for velocities), 2) significant velocity perturbations up to 1 rad / sec after each ground impact, 3) model parameter estimation error of up to 1cm in the main body COM position, and 4) delays of up to 0.04 seconds. In this section we will show some results of stabilization on two example terrains: bounding up stairs, and bounding over logs.

Since the impact map is the most sensitive and difficult-to-model phase of the dynamics, we can demonstrate the effectiveness of the controller by adding normally-distributed random angular velocity perturbation to the passive (stance-ankle) joint after each impact. Figure 6-1 shows example trajectories of LittleDog bounding up stairs (perturbations with standard deviation of 0.2 rad/sec), and Figure 6-3 shows it bounding over logs (perturbations with standard deviation of 0.1 rad/sec).

In each figure, the trajectory of the center of mass is plotted for three cases: 1) the nominal (unperturbed) motion, as computed by the RRT planner, 2) running the

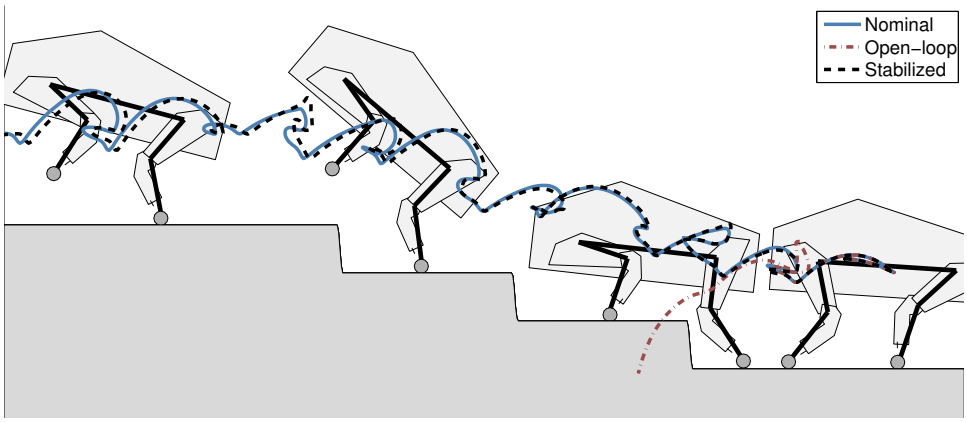

Figure 6-1: Bounding up steps in simulation
Cartoon of bounding up steps with center-of-mass trajectories indicated for nominal, open-loop with perturbations, and stabilized with perturbations.

nominal control inputs open-loop with passive-joint velocity perturbations, and 3) the transverse-LQR stabilized robot with the same perturbations. One can see that for both terrains, after the first perturbation, the open-loop robot deviates wildly and falls over. This shows the inherent instability of the motion. In contrast, the stabilized version is able to remain close to the nominal trajectory despite the perturbations.

We analyze this behavior in more detail in Figure 6-2. Here we depict the phase portrait of the COM angle θ and its derivative $\dot{\theta}$ during a single bound for the same three cases. This coordinate is not directly actuated, and can only be controlled indirectly via the actuated joints. Note that the nominal trajectory comes quite close to the state $\theta = \frac{\pi}{2}$, $\dot{\theta} = 0$. This state corresponds to the robot being balanced upright like an inverted pendulum, and is an unstable equilibrium (c.f. the separation of trajectories in Figure 3-5). One can see that when running open-loop, a small perturbation in velocity pushes the robot to the wrong side of this equilibrium, and the robot falls over. In contrast, the transverse-LQR stabilized robot moves back towards the nominal trajectory.

6.1.2 In Feedback with Estimator

The Lightweight Communications and Marshalling, which we use for communication between all real-time modules (see Figure 4-1), abstracts the interfaces between dif-

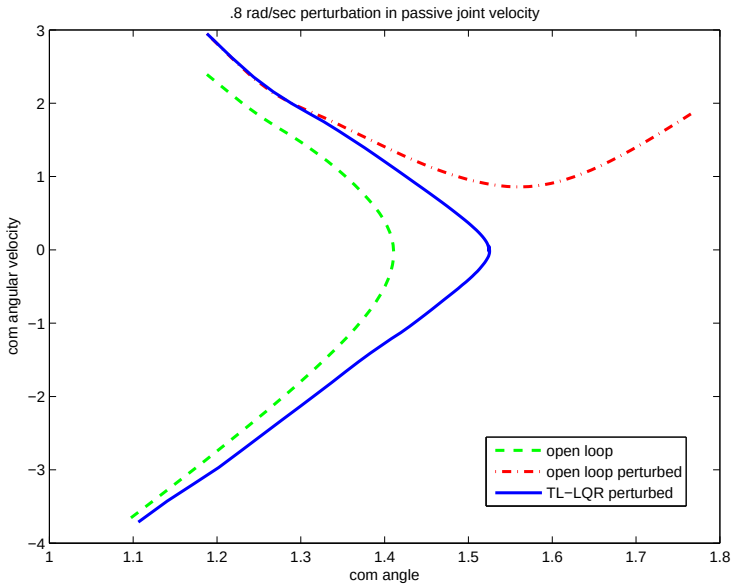

Figure 6-2: Phase portrait for a bounding motion
Phase portrait of COM angle θ vs its derivative $\dot{\theta}$ for 1) a nominal half-bound trajectory, 2) open loop execution with perturbation of +0.8 rad/sec in the initial condition, and 3) transverse-LQR stabilized trajectory with perturbed initial state.

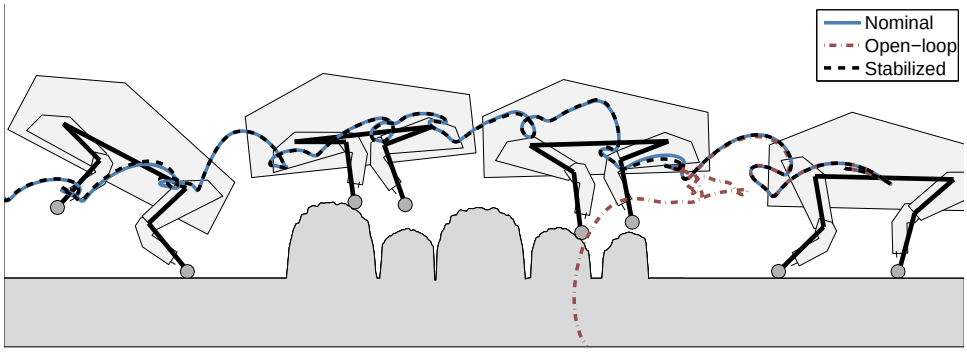

Figure 6-3: Bounding over logs in simulation
Cartoon of bounding over logs with center-of-mass trajectories indicated for nominal, open-loop with perturbations, and stabilized with perturbations.

ferent blocks, allowing us to swap between the real LittleDog robot and the model without any changes to the other modules. Using that feature, we simulated LittleDog with the estimator in feedback with the controller and simulated delays in the model, with exactly the control loop that would be used on the real robot.

Even with no process or sensor noise (with the communication module providing some stochasticity), the performance degrades dramatically when using the estimator in feedback with the controller as opposed to using perfect state knowledge for control. Some of the failure modes include the dynamics not advancing in phase and the robot getting stuck in double support phase, the robot falling over backwards, the robot shaking with increasing amplitude, and foot slipping, especially when coupled with shaking of the robot. Most of these involve the states separating far from the nominal trajectory, which usually can be seen on the COM angle versus COM angular velocity plots, except when most of the oscillation is happening at the robot's joints. Even after a large amount of manually tuning the parameters of the controller and the estimator to improve the success rate, it was still rare for the simulation to execute a successful bounding trajectory. One can eliminate almost any of the failure modes by taking a set of parameters to an extreme, but that results in other failure modes becoming more frequent. For example, oscillations in the phase typically arise because of feedback driven by the noise in the estimates of the COM angular velocity. However, lowering its weight in the phase computation tends to result in inaccurate phase estimates when the COM angular velocity is close to zero and increases the frequency with which the robot flips over.

Figures 6-4 and 6-5 show the phase estimate and trajectory segments for a typical such simulation with the control, estimation, and model elements in feedback. The top plot on the trajectory figure corresponds to the segment with phase 48 through 99, the middle plot corresponds to the segment with phase 101 through 136, while the bottom plot corresponds to the segment with phase 141 through 184. The small gaps between these segments, as well as phase 1 through 47, correspond to segments in double support mode.

The simulated robot is in double support mode until phase 47 and, while the

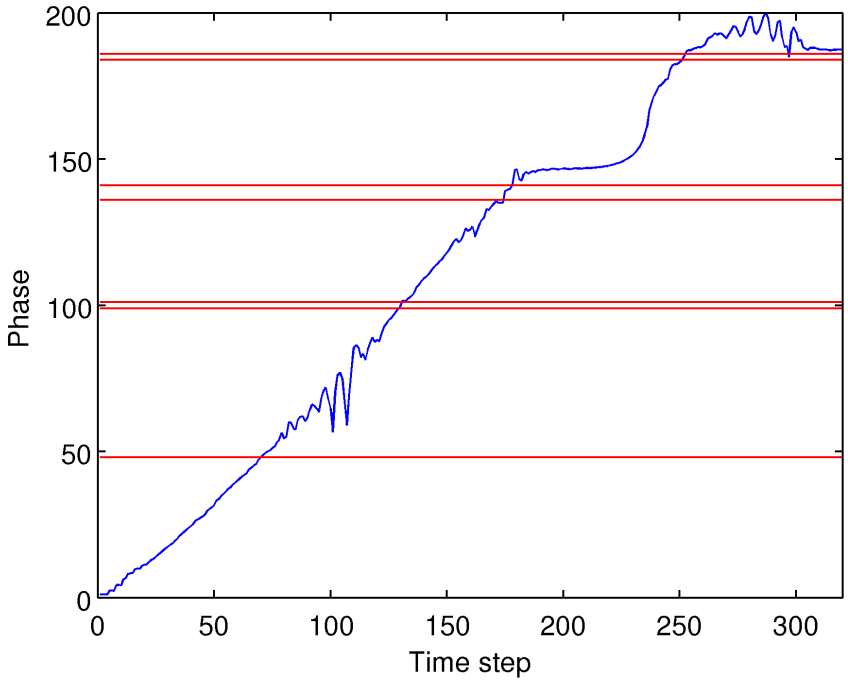

Figure 6-4: Phase for a close-loop simulation with feedback controller and estimator Typical phase plot for an unsuccessful bounding attempt in simulation with full delays, feedback controller, and estimator. Red lines indicate the phase transition times, as detected by the estimator. The oscillation at around timestep 100 is caused by foot slip and oscillations in the joint control commands and positions. At around time step 200 the robot almost flips, but is able to recover. At around timestep 250 the robot's foot bounces on contact with the ground, causing it to prematurely enter into double support, from which it can't recover.

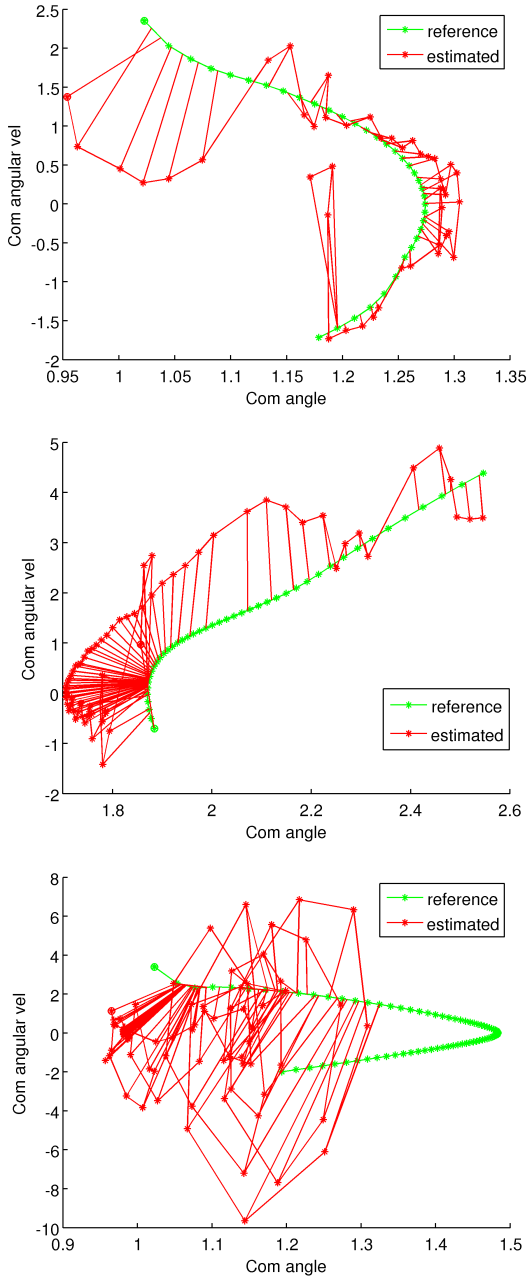

Figure 6-5: Trajectory segments for a closed-loop control and estimator simulation

Trajectory segments in COM angle and COM angular velocity coordinates, with top, middle, and bottom corresponding with phase 48 through 99, 101 through 136, and 141 through 184 in figure 6-4, respectively.

increase in the phase is monotonic, the slope of the phase averages at 0.69 instead of 1, which indicates that the feedforward term is lagging slightly. In the next segment, where the robot lifts itself up on the back legs, the foot of the robot slips on the ground and there is a lot of shaking in the legs, which explains the rapidly jumping around estimated state trajectory and oscillations in the phase. Oscillations in the joints produce sharp increases in force at the ground and make the feet more likely to slip, while foot slip causes the robot to sharply deviate from nominal trajectory and results in large command changes to the joints. However, it is not clear which one of these initiates the feedback cycle, which appears and disappears suddenly because foot slip is a discrete event.

In the next segment the robot is on the front feet between phase 101 through 136, corresponding to the middle plot in Figure 6-5. The trajectory doesn't stay close to the nominal, but doesn't diverge either, and, except for a few outliers and some jumps towards the end, the controller performs decently on this segment. After the collision and transition to the back feet, the robot barely recovers from falling backwards, which is seen as a small slope on the phase plot and as a large clump of states between COM angles of 0.95 and 1.00. The lowest two angles for points on the nominal trajectory are 1.00 and 1.05, so it is a significant difference in angle. The robot manages to make it to the next collision, where the foot slips and bounces, because the robot is in the wrong state at the moment of ground contact. After the bounce the robot doesn't have enough momentum to roll onto the front foot and continue, so the bounding terminates, as can be seen from the flat-lining phase plot.

6.2 Experimental Results

6.2.1 Open Loop

As discussed in Chapter 3, the model dynamics are not stable around the bounding trajectories of the robot and even those trajectories generated by identical command sequences with closely repeated initial conditions diverge quickly. Therefore, one can't

expect a planned trajectory to be successful on the robot without feedback.

However, for some trajectories and initial conditions, it should be possible to have the robot perform a few bounds without feedback. With some tuning, we were able to produce bounding over a log terrain on the real robot, shown in Figure 6-6, which had approximately a 20% success rate, even though the robot was carefully positioned to be in the same configuration at the start of each trial.

In addition, we were able to produce a number of open loop trajectories that could produce several bounds on flat terrain.

6.2.2 With Feedback Control

So far, none of our attempts to produce stable bounding of LittleDog from RRT planned trajectories have been successful. It is important to note that the failure modes on the actual robot match those observed in simulation, discussed in the section above, including the robot's behavior and the phase computations. One common failure mode involves feedback between phase and the joint velocities, which are coupled by the phase computations and the controller, and are driven by the measurement noise and delays. The oscillations do not occur if any of the last 4 factors are absent in the simulation, but it is impossible to not have them when implementing the bounding algorithm on the physical LittleDog robot. As shown in Figure 6-7, they have a similar frequency and amplitude for both the simulated and the physical robot.

For these reasons, we believe that the closed-loop system describes the actual bounding LittleDog sufficiently accurately. To achieve stable bounding efforts should be directed to make the simulated feedback loop more robust by improving primarily the control and estimation components. Currently, while the individual components seem to work well, their interaction in simulation is largely responsible for the failure of bounding control.

Figure 6-6: Open-loop bounding over logs with LittleDog

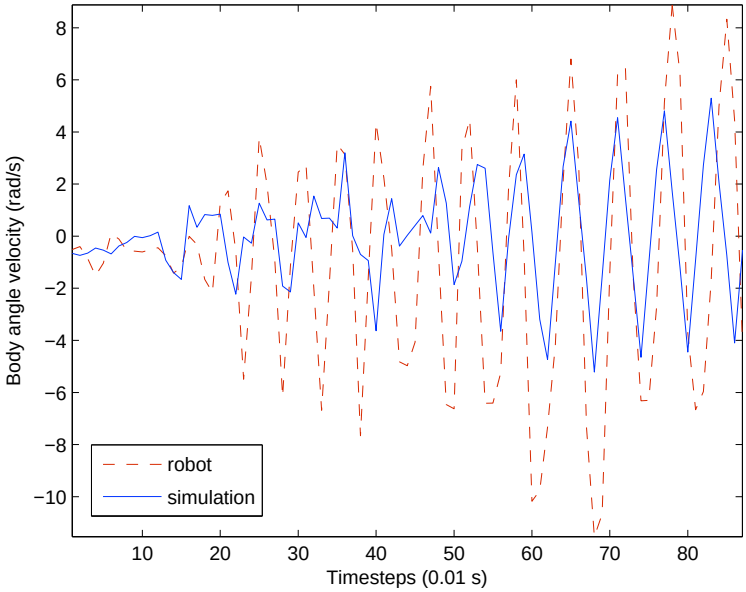

Figure 6-7: Oscillations induced by measurement noise and delays
Body angle velocity, also known as COM velocity, can oscillate uncontrollably in both the simulation and on the real robot in the presence of sensor noise and delays.

Chapter 7

Summary and Discussion

In this work, we have put together a framework for achieving a stable bounding gait of the LittleDog robot over rough terrain. We have chosen a model-based control approach and have developed and identified an accurate planar physics-based model of LittleDog. The model describes the motions in the joints of the robot and includes a novel method for ground contact modeling that explicitly incorporates the springs in the feet of LittleDog. We then altered the Extended Kalman Filter algorithm to explicitly incorporate the time delays present in the robot's sensors and used it, along with the model, to construct a state estimator for the robot. We applied a transverse linearization controller to trajectories planned using the model, adapting the controller as necessary to the specifics of having non-negligible time discretization of motor inputs. We then integrated the controller, estimator, and dynamical model in simulation, analyzed the system and tuned the components to improve performance in hopes of transferring it over to the real system.

The model developed, while not perfect, provides an accurate description of the system's robot dynamics and even allowed us to generate trajectories that produced short bounding motions on LittleDog with no feedback. The transverse linearization controller was highly successful in stabilizing the system in simulation with perfect state knowledge. The estimator also shows reasonable ability to track the states of the system and compensate for delays. Unfortunately, when the components get combined into a feedback loop in simulation, we are not able to produce a stable

bounding motion, largely because of the harmful interactions between the estimation and feedback control algorithms. Implementing these algorithms on the real robot instead of simulation produces similar behavior in terms of the failure modes of the system. So, we believe that we can achieve bounding on the actual LittleDog robot by making the individual components of our control framework more robust and by minimizing the harmful interaction between them.

The model was developed with the goal of finding a balance between accuracy and complexity, which mostly relates to state space dimension, in this case. While higher levels accuracy can be achieved by including the unmodeled effects of backlash in the joints, joint loading from external forces, and improvements in ground interactions modeling, particularly in the friction model, all of these improvements would come at increased complexity for the purposes of planning, estimation, and feedback control.

Currently, the estimator does not use the force sensors in the feet of LittleDog, which would help in detecting the moment of collision with the ground, an important time for the control system. Obviously, the accuracy of the estimates, and with it the whole control loop performance, will improve significantly by using sensors with lower delays and smaller noise.

There is more room for improvement in the control algorithm. In this work, we only started to investigate the effects of having large control time steps for transverse linearization, and more rigorous theoretical understanding is desired to learn how to best adapt this technique to these types of systems. The weight matrix, W, used in the definition of the transverse surfaces was constant, and we expect a significant improvement from applying a good method of varying W along the trajectory or from constructing the surfaces by directly choosing the orthogonal vector, instead of using the direction of the dynamics. Finally, note that the finite-time LQR gains were computed for each segment separately. If the transverse dynamics and collision gradients are sufficiently reliable, it might be better to compute the solution to the Riccati equation for LQR across multiple collisions. Above all, what is needed is a better understanding of the interactions between the estimator and control algorithm in a complex dynamical system like LittleDog. This would allow a more intelligent

selection of the LQR and Kalman Filter gains, which are now designed independently of each other, to minimize harmful effects and make the overall system more robust.

Although the focus of this work was on the specific task of designing and stabilizing LittleDog bounding trajectories, the approach that was used is very general and could be applied to controlling many systems, particularly other walking robots, potentially only by swapping out the dynamics model and changing the estimator to fit the specifics of the new system. We hope that the work presented here along with potential improvements listed above would be sufficient in order to solve, or at least bring closer to solution, truly dynamic locomotion over arbitrary rough terrain on LittleDog and many other robots.

Appendix A

Control Verification

The robustness of a transverse verification controller will be limited by the region of validity of the transverse coordinates and by the error introduced during linearization of the dynamics. Estimating the robustness of this approach on the LittleDog robot currently requires extensive simulation with various initial conditions and perturbations. Because of the high complexity of the problem, it requires an unreasonable number of computation to generate an accurate estimate. It would be preferable to have an algorithm that produces robustness guarantees as the controller is generated, simplifying the analysis and opening the possibility of optimizing over the size of the controller's basin of attraction. In pursuit of that goal, we have analyzed the basin of attraction of the simplest walking system, the Rimless Wheel.

A.1 Rimless Wheel Dynamics

The rimless wheel is a simple planar model of walking and consists of a central mass with several 'spokes' extending radially outward. (See Figure A-1). At any given moment one of the spokes is pinned at the ground, and the system follows the dynamics of a simple pendulum, $f(\theta, \dot{\theta}) = [\dot{\theta}, \sin(\theta)]'$. When another spoke contacts the ground, the system undergoes an inelastic collision governed by $\dot{\theta}^+ = \cos(2\alpha)\dot{\theta}$, and the new spoke becomes the pinned one.

On a sufficiently inclined slope the system has a stable limit cycle, for which the

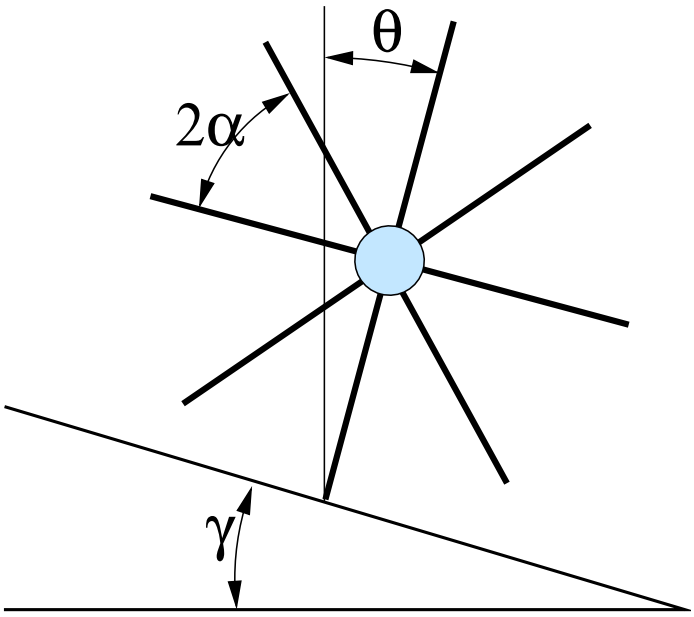

Figure A-1: Rimless wheel system

energy lost in collision is perfectly compensated by the change in potential energy. The rimless wheel has been analyzed in the literature and the basin of attraction has been computed exactly (see [7]).

Figure A-2 shows the phase portrait of the rimless wheel, with arrows indicating the direction of the dynamics. The right edge of the graph represents the collision surface that maps to the left edge of the graph (or vice-versa, depending on the direction of dynamics). Because the impact depends only on the value of the angle, θ, and not on $\dot{\theta}$, the collision surfaces are vertical. The thick green lines are the homoclinic orbits of the simple pendulum. The thick black line shows the stable limit cycle, and the shading shows a subset of its true region of attraction.

The hybrid dynamics in this one degree of freedom system make it a good first step in developing an algorithm for analyzing the basin of attraction in more general walking systems, and the analytically computed basin presents a good metric for its performance.

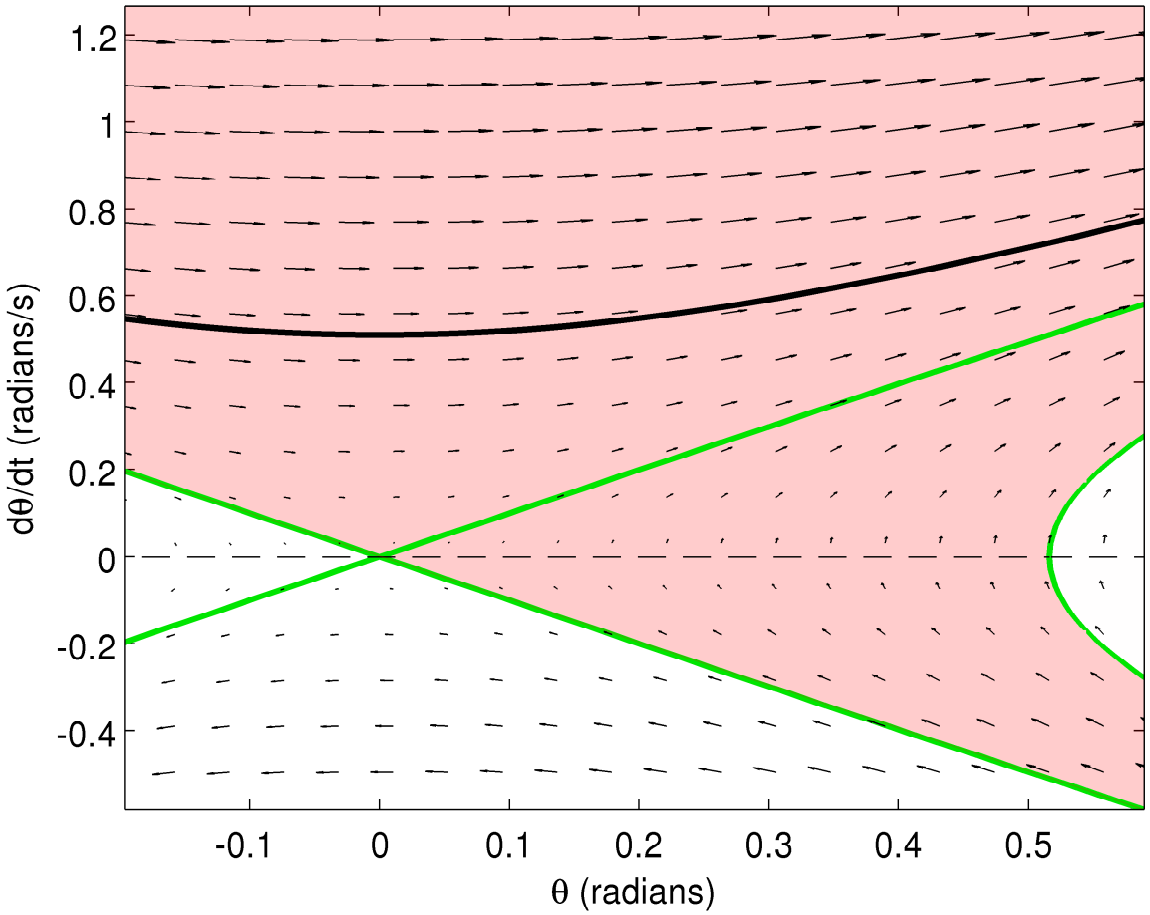

Figure A-2: Phase portrait of the rimless wheel system.

A.2 Transverse Verification

The verification of orbital stability relies on the construction of transverse coordinates, as described in Chapter 5, and is outlined in detail in [23] and [25]. Given an orbit of the rimless wheel $x^\star(\cdot)$, the method computes a region of state space, where all initial conditions are guaranteed to be orbitally stable. The method relies on the construction of a local coordinate change along every point of the orbit and then constructing a Lyapunov function candidate on bounded regions of the transversal planes. A key limitation of the method is that the mapping needs to be one-to-one in the verified regions, as an intersection of transversal surfaces produces a singularity in the equations.

For the rimless wheel, it is natural to select vertical transversal surfaces, since there are no singularities in the change of variables, and the transversal surfaces are aligned with switching surfaces. The surfaces can be parametrized by θ as $\tau = \tau(\theta)$, and the nominal trajectory is simply $\theta^\star(\theta) = \theta$ and $\dot{\theta}^\star(\theta) = \sqrt{2E - 2\cos(\theta)}$, where E is the total energy of the system. Then the transversal coordinate is the vertical position with respect to the nominal trajectory: $x_\perp = \dot{\theta} - \dot{\theta}^\star(\theta)$.

To find an initial candidate Lyapunov function we computed the unique periodic solution of the jump Lyapunov differential equation

$$\begin{aligned} -\dot{P}(t) &= A(t)'P(t) + P(t)A(t) + Q,\ t \neq t_i \\ P(\tau_i^-) &= A_d(\tau_i)'P(\tau_i^+)A_d(\tau_i) + Q_i,\ t = t_i \end{aligned}$$

where $Q, Q_i > 0$, $A(t)$ is the gradient of the dynamics and $A_d(\tau_i)$ is a projection matrix representing the collision dynamics. We then searched over scalar rescalings $V(x) = (1/\sigma)x'_\perp P(\tau)x_\perp$, where σ is a polynomial.

Figure A-3 shows the results for a scalar σ. The discrete set of transverse surfaces can be seen as thin black vertical lines around the orbit. The computed basin of attraction (dark shading) is within the true basin (light shading), but doesn't fill it fully. This is not surprising, since we searched over a very restrictive set of Lyapunov functions.

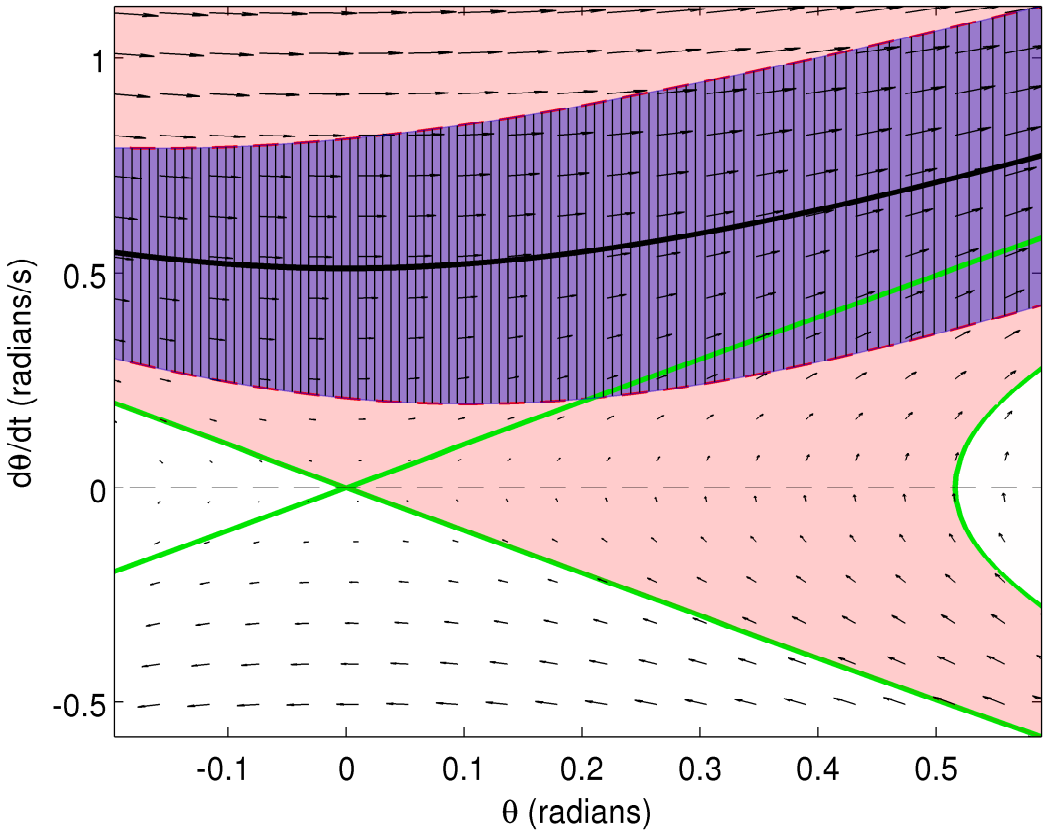

Figure A-3: Regions of Attraction for the rimless wheel limit cycle.
Light shaded region is the true RoA. Dark shaded region is the verified RoA.

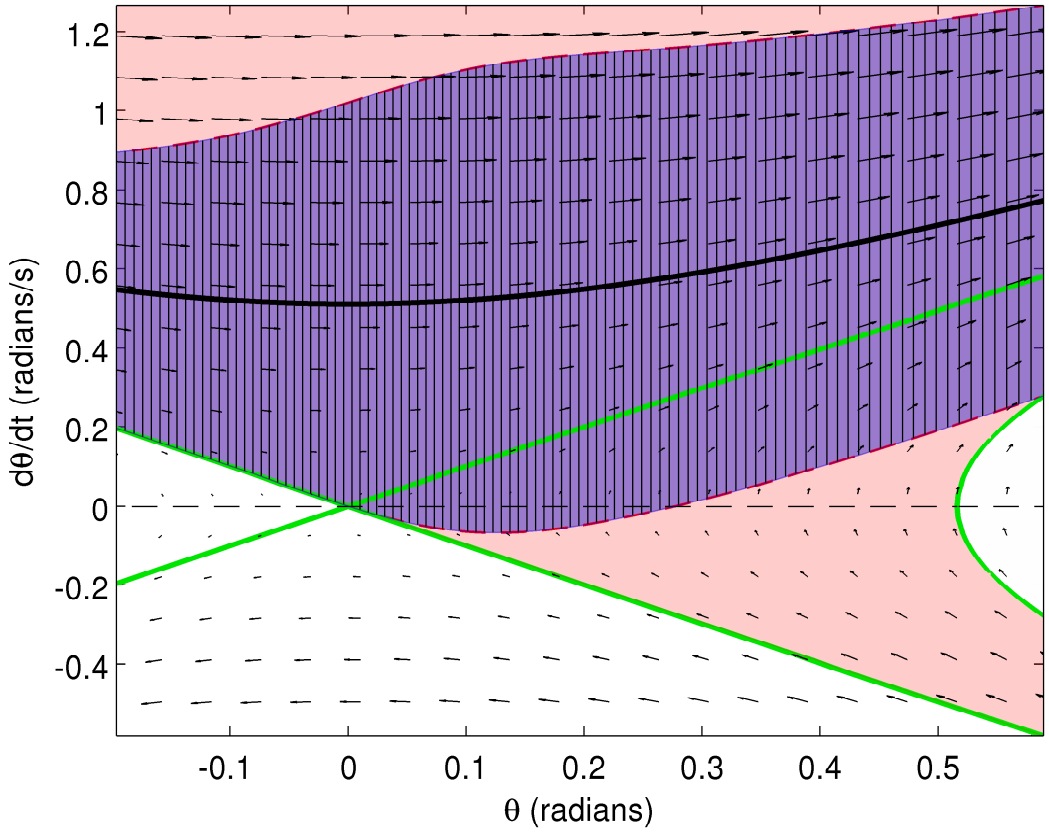

Figure A-4: Regions of Attraction for the rimless wheel limit cycle.
Light shaded region is the true RoA. Dark shaded region is the verified RoA.

We then searched over 10^{th}-order rescaling polynomials $\sigma(\tau)$, to maximize the area of the computed region. Figure A-4 shows the results and, as expected, the basin of attraction is larger.

Note that the verified basin of attraction includes regions where $\dot{\theta} < 0$ and, by the choice of transverse surfaces, $\dot{\tau} < 0$. The verification procedure still holds when the system state moves backwards through the transverse surfaces.

A.3 Future directions

The above procedure demonstrates an approach for computing a guaranteed basin of attraction for orbits of walking systems with collisions. The same method has

also been applied to the compass gait system in [25]. Scaling it up to more complex systems such as LittleDog presents significant challenges, because of high number of dimensions and the necessity of polynomial approximation to the dynamics, but is an interesting direction of research for the future.

Bibliography

[1] F. Asano, M. Yamakita, N. Kamamichi, and Luo Zhi-Wei. A novel gait generation for biped walking robots based on mechanical energy constraint. *IEEE Transactions of Robotics and Automation*, 20(3):565–573, June 2004.

[2] Andrzej Banaszuk and John Hauser. Feedback linearization of transverse dynamics for periodic orbits. *Systems & Control Letters*, 26(2):95 – 105, 1995.

[3] Pedro Berges and Alan Bowling. Rebound, slip, and compliance in the modeling and analysis of discrete impacts in legged locomotion. *Journal of Vibration and Control*, 12(12):1407 – 1430, 2006.

[4] Katie Byl, Alexander Shkolnik, Sam Prentice, Nicholas Roy, and Russ Tedrake. Reliable dynamic motions for a stiff quadruped. In *Proceedings of the 11th International Symposium on Experimental Robotics (ISER)*, Athens, Greece, July 2008.

[5] Catlin and D.E. *Estimation, control, and the discrete Kalman filter*. Applied mathematical sciences. Springer-Verlag, 1989.

[6] C. Chevallereau, G. Abba, Y. Aoustin, F. Plestan, E. R. Westervelt, C. Canudas-De-Wit, and J. W. Grizzle. Rabbit: a testbed for advanced control theory. *IEEE Control Systems Magazine*, 23(5):57–79, Oct. 2003.

[7] Michael J. Coleman. *A Stability Study of a Three-Dimensional Passive-Dynamic Model of Human Gait*. PhD thesis, Cornell University, 1998.

[8] Steven H. Collins, Andy Ruina, Russ Tedrake, and Martijn Wisse. Efficient bipedal robots based on passive-dynamic walkers. *Science*, 307:1082–1085, February 18 2005.

[9] G. Gilardi and I. Sharf. Literature survey of contact dynamics modelling. *Mechanism and Machine Theory*, 37(10):1213 – 1239, 2002.

[10] Goswami, Ambarish, Espiau, Bernard, Keramane, and Ahmed. Limit cycles in a passive compass gait biped and passivity-mimicking control laws. *Autonomous Robots*, 4:273–286, 1997. 10.1023/A:1008844026298.

[11] Ambarish Goswami, Benoit Thuilot, and Bernard Espiau. A study of the passive gait of a compass-like biped robot: symmetry and chaos. *International Journal of Robotics Research*, 17(12), 1998.

[12] J.W. Grizzle, G. Abba, and F. Plestan. Asymptotically stable walking for biped robots: analysis via systems with impulse effects. *IEEE Transactions on Automatic Control*, 46(1):51–64, Jan. 2001.

[13] Jack K. Hale. *Ordinary Differential Equations*. Robert E. Krieger Publishing Company, New York, 1980.

[14] Masato Hirose and Kenichi Ogawa. Honda humanoid robots development. *Philosophical Transactions of the Royal Society*, 365(1850):11–19, Jan 2007.

[15] Albert S. Huang, Edwin Olson, and David C. Moore. Lcm: Lightweight communications and marshalling. *International Conference on Intelligent Robots and Systems (IROS), 2010 IEEE/RSJ*, pages 4057–4062, October 2010.

[16] K. H. Hunt and F. R. E. Crossley. Coefficient of restitution interpreted as damping in vibroimpact. *Journal of Applied Mechanics*, 42 Series E(2):440–445, 1975.

[17] Fumiya Iida and Russ Tedrake. Minimalistic control of a compass gait robot in rough terrain. In *Proceedings of the IEEE/RAS International Conference on Robotics and Automation (ICRA 09)*, Kobe, Japan, May 2009. IEEE/RAS.

[18] Kajita, S. Kanehiro, F. Kaneko, K. Fujiwara, K. Harada, K. Yokoi, K. Hirukawa, and H. Resolved momentum control: humanoid motion planning based on the linear and angular momentum. *Intelligent Robots and Systems (IROS), Proceedings*, 2003.

[19] S. Kajita, F. Kanehiro, K. Kaneko, K. Fujiware, K. Harada, K. Yokoi, and H. Hirukawa. Biped walking pattern generation by using preview control of zero-moment point. In *Proceedings of the IEEE/RAS International Conference on Robotics and Automation (ICRA 03)*, pages 1620–1626, Taipei, Taiwan, September 2003. IEEE.

[20] Mrinal Kalakrishnan, Jonas Buchli, Peter Pastor, Michael Mistry, and Stefan Schaal. Learning, planning, and control for quadruped locomotion over challenging terrain. *I. J. Robotic Res.*, 30(2):236–258, 2011.

[21] Kenji Kaneko, Fumio Kanehiro, Shuuji Kajita, Hirohisa Hirukawa, Toshikazu Kawasaki, Masaru Hirata, Kazuhiko Akachi, and Takakatsu Isozumi. Humanoid robot HRP-2. In *Proceedings of the IEEE/RAS International Conference on Robotics and Automation (ICRA 04)*, pages 1083–1090, New Orleans, LA, May 2004. IEEE.

[22] J. Zico Kolter and Andrew Y. Ng. The stanford littledog: A learning and rapid replanning approach to quadruped locomotion. *I. J. Robotic Res.*, 30(2):150–174, 2011.

[23] Ian R. Manchester. Transverse dynamics and regions of stability for nonlinear hybrid limit cycles. *Proceedings of the 18th IFAC World Congress, extended version available online: arXiv:1010.2241 [math.OC]*, Aug-Sep 2011.

[24] Ian R. Manchester, Uwe Mettin, Fumiya Iida, and Russ Tedrake. Stable dynamic walking over rough terrain: Theory and experiment. In *Proceedings of the International Symposium on Robotics Research (ISRR)*, Lucerne, Switzerland, Aug. 2009.

[25] Ian R. Manchester, Mark M. Tobenkin, Michael Levashov, and Russ Tedrake. Regions of attraction for hybrid limit cycles of walking robots. *Proceedings of the 18th IFAC World Congress, extended version available online: arXiv:1010.2247 [math.OC]*, 2011.

[26] D.W. Marhefka and D.E. Orin. Simulation of contact using a nonlinear damping model. In *Proceedings of the IEEE/RAS International Conference on Robotics and Automation (ICRA 96)*, volume 2, pages 1662–1668 vol.2, Minneapolis, MN, USA, Apr 1996.

[27] Matveev, A. S. Savkin, and A. V. The problem of state estimation via asynchronous communication channels with irregular transmission times. *IEEE Transactions on Automatic Control*, 48(4):670–675, 2003.

[28] David Q. Mayne, James B. Rawlings, Christopher V. Rao, and P. O. M. Scokaert. Constrained model predictive control: Stability and optimality. *Automatica*, 36(6):789–814, 2000.

[29] Tad McGeer. Passive dynamic walking. *International Journal of Robotics Research*, 9(2):62–82, April 1990.

[30] Murphy, Michael P., Saunders, Aaron, Moreira, Cassie, Rizzi, Alfred A., Raibert, and Marc. The littledog robot. *Int. J. Rob. Res.*, 30:145–149, February 2011.

[31] Peter D. Neuhaus, Jerry E. Pratt, and Matthew J. Johnson. Comprehensive summary of the institute for human and machine cognition's experience with littledog. *I. J. Robotic Res.*, 30(2):216–235, 2011.

[32] Petersen, I.R., Ugrinovskii, V.A., Savkin, and A.V. *Robust control design using H-8 methods*. Communications and control engineering series. Springer, 2000.

[33] James Pippine, Douglas Hackett, and Adam Watson. An overview of the defense advanced research projects agency's learning locomotion program. *I. J. Robotic Res.*, 30(2):141–144, 2011.

[34] Dimitris Pongas, Michael Mistry, and Stefan Schaal. A robust quadruped walking gait for traversing rough terrain. *Proceedings of the IEEE/RAS International Conference on Robotics and Automation (ICRA 07)*, April 2007.

[35] Marc Raibert, Kevin Blankespoor, Gabriel Nelson, Rob Playter, and the BigDog Team. Bigdog, the rough-terrain quadruped robot. *Proceedings of the 17th World Congress, The International Federation of Automatic Control*, Jul. 2008.

[36] Marc H. Raibert. *Legged Robots That Balance*. The MIT Press, 1986.

[37] M.H. Raibert, M. Chepponis, and H.B. Brown. Running on four legs as though they were one. *IEEE Journal of Robotics and Automation*, 2(2):70–82, 1986.

[38] C. David Remy. *Optimal Exploitation of Natural Dynamics in Legged Locomotion*. PhD thesis, ETH ZURICH, 2011.

[39] Y. Sakagami, R. Watanabe, C. Aoyama, S. Matsunaga, and N. Higakiand K. Fujimura. The intelligent ASIMO: system overview and integration. In *Proceedings of the IEEE/RSJ International Conference on Intelligent RObots and Systems (IROS 02)*, volume 3, pages 2478 – 2483, Switzerland, September 2002. IEEE.

[40] Y. Sawaragi, T. Katayama, and Satoru Fujishige. Sequential state estimation with interrupted observation. *Information and Control*, 21(1):56–71, August 1972.

[41] A. L. Schwab and M. Wisse. Basin of attraction of the simplest walking model. *Proceedings of the ASME Design Engineering Technical Conference*, 6:531–539, Sep 2001.

[42] Shiriaev, A., Perram, J.W., Canudas de Wit, and C. Constructive tool for orbital stabilization of underactuated nonlinear systems: Virtual constraints approach. *Automatic Control, IEEE Transactions on*, 50(8):1164–1176, Aug. 2005.

[43] Anotn S. Shiriaev, Leonid B. Freidovich, and Ian R. Manchester. Can we make a robot ballerina perform a pirouette? orbital stabilization of periodic motions of underactuated mechanical systems. *Annual Reviews in Control*, 32(2):200–211, Dec 2008.

[44] Shkolnik, A., Byl, K., Rohanimanesh, K., Roy, N., Tedrake, and R. Walking on rough terrain with a position controlled quadruped robot. In *International Workshop on Legged Locomotion for Young Researchers*, Cambridge, MA, 2007.

[45] Alexander Shkolnik. *Sample-Based Motion Planning in High-Dimensional and Differentially-Constrained Systems*. PhD thesis, MIT, February 2010.

[46] Alexander Shkolnik, Michael Levashov, Ian R. Manchester, and Russ Tedrake. Bounding on rough terrain with the littledog robot. *The International Journal of Robotics Research (IJRR)*, 30(2):192–215, Feb 2011.

[47] M W Spong and F Bullo. Controlled symmetries and passive walking. *IEEE Transactions on Automatic Control*, 50(7):1025–1030, Jul 2005.

[48] Russ Tedrake, Ian R. Manchester, Mark M. Tobenkin, and John W. Roberts. LQR-Trees: Feedback motion planning via sums of squares verification. *International Journal of Robotics Research*, 29:1038–1052, July 2010.

[49] Nan-Chyuan Tsai, Ray, and A. Compensatability and optimal compensation under randomly varying distributed delays. In *Decision and Control, 1998. Proceedings of the 37th IEEE Conference on*, volume 1, pages 772 –777 vol.1, 1998.

[50] Miomir Vukobratovic and Branislav Borovac. Zero-moment point - thirty five years of its life. *International Journal of Humanoid Robotics*, 1(1):157–173, 2004.

[51] E. R. Westervelt, J. W. Grizzle, and D. E. Koditschek. Hybrid zero dynamics of planar biped walkers. *IEEE Transactions on Automatic Control*, 48(1):42–56, Jan 2003.

[52] Eric R. Westervelt, Jessy W. Grizzle, Christine Chevallereau, Jun Ho Choi, and Benjamin Morris. *Feedback Control of Dynamic Bipedal Robot Locomotion*. CRC Press, Boca Raton, FL, 2007.

[53] Matthew Zucker, Nathan D. Ratliff, Martin Stolle, Joel E. Chestnutt, J. Andrew Bagnell, Christopher G. Atkeson, and James Kuffner. Optimization and learning for rough terrain legged locomotion. *I. J. Robotic Res.*, 30(2):175–191, 2011.